J Mater Sci (2008) 43:5395–5429
DOI 10.1007/s10853-008-2749-0

REVIEW

Advances in the application of nanotechnology in enabling a 'hydrogen economy'

Uttara Sahaym · M. Grant Norton

Received: 6 May 2008 / Accepted: 22 May 2008 / Published online: 28 June 2008

Abstract Hydrogen is gaining a great deal of attention as an energy carrier as well as an alternative fuel. However, in order to fully implement the so called 'hydrogen economy' significant technical challenges need to be overcome in the fields of production and storage of hydrogen and its point of use especially in fuel cells for the automotive industry. The purpose of this review is to present and discuss recent advances in the use of nanomaterials for solar hydrogen production and on-board solid state storage of hydrogen. The role of nanotechnology in enhancing the efficiency of fuel cells and reducing their cost is also discussed.

Introduction

Supply and demand of energy determine the course of global development in every sphere of human activity. The world's energy need is certain to increase with growth in population. We now use 4.1×10^{20} J of energy per year, which is equivalent to 13 TW of power. This consumption may more than double to ~30 TW by the year 2050 and then triple ~46 TW by the end of the century. The reserves of fossil fuels are not sufficient. Moreover, their continued use produces harmful side effects such as pollution, which threatens human health and greenhouse gases that are associated with global climate change. Alternative renewable fuels are at present not competitive with fossil fuels in terms of cost and production capacity. Finding viable alternative sources of clean energy to satisfy the projected demand (double and triple of today's energy demand) is one of the big challenges of society.

It is essential to develop alternative energy approaches especially for transportation not only to replace rapidly depleting oil reserves, but also to limit the effects of global warming by reducing the atmospheric emission of carbon dioxide [1–5]. Hydrogen is gaining increasing attention, both politically and scientifically, and is considered one of the most promising energy carriers [6]. Some examples where hydrogen can be used are:

- Fuel in internal combustion engines (ICE)
- Energy carrier in fuel cell vehicles (FCV)
- Electrical energy storage for stationary applications

Interest in the use of hydrogen is based on its clean burning qualities, its potential for domestic production, and high efficiency of FCV (~2–3 times that of conventional gasoline ICE) [1]. Hydrogen is one of the most abundant elements on earth and when used in a fuel cell, the sole by-product is water.

Figure 1 illustrates the 'hydrogen economy' as a network of primary energy sources linked to multiple end-uses through hydrogen as an energy carrier. Hydrogen can be produced using any of the primary energy sources such as fossil, nuclear, and renewable. The energy needed for transportation applications and electricity for stationary applications is derived from reacting hydrogen with oxygen. However, in order to implement the hydrogen economy and completely replace fossil fuels, there are significant technical challenges that need to be overcome in each of the following areas:

- Production and generation
- Storage
- Conversion to electrical energy and heat at the point of use

U. Sahaym (✉) · M. G. Norton
Washington State University, Pullman, WA, USA
e-mail: usahaym@wsu.edu

M. G. Norton
e-mail: mg_norton@wsu.edu

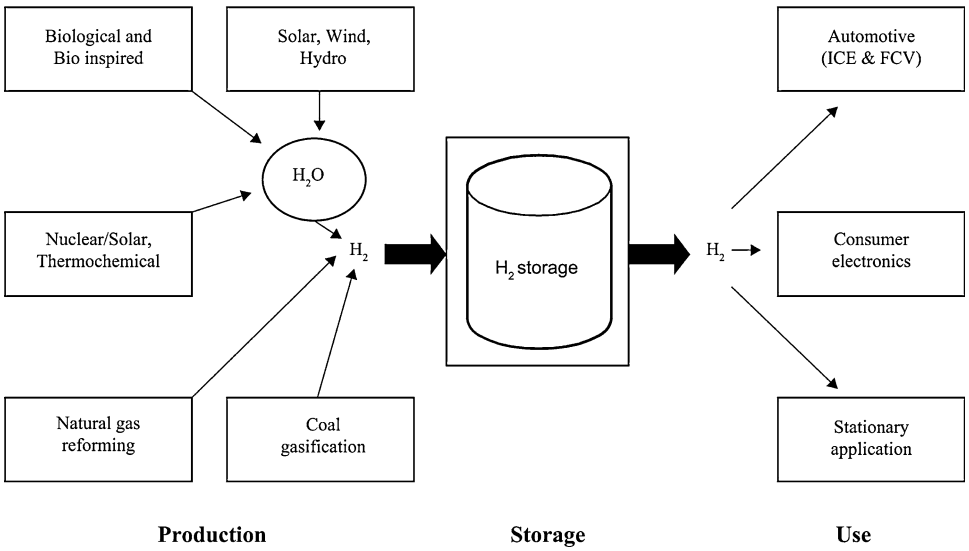

Fig. 1 Hydrogen economy as a network of primary energy sources linked to various end-uses through hydrogen as an energy carrier

All the technical barriers hinge on understanding and controlling atomic and molecular level processes at the interface between hydrogen and various materials. Nanoscale materials would appear ideally suited for overcoming these barriers because of their enormous surface areas. The performance of catalysts, hydrogen storage materials, and electrode assemblies for fuel cells can all be enhanced by the use of nanoscale processes and architectures. Hence, the research needs of hydrogen economy resonate with compelling developments in nanotechnology. This review presents and discusses recent advances in the application of nanotechnology toward enabling the hydrogen economy. It addresses some of the challenges and research needs related to production and storage of hydrogen, and its point of use especially in fuel cells for the automotive industry.

Hydrogen production

Although hydrogen is an attractive replacement for fossil fuels, it does not occur in nature as the molecule H_2. Rather, it occurs bound in chemical compounds such as water or hydrocarbons that must be chemically transformed to yield H_2. Hydrogen can be produced using diverse domestic resources including fossil fuels, such as natural gas and coal, nuclear, hydroelectric, biomass, and renewable sources such as wind, solar, and geothermal as illustrated in Fig. 2.

Steam reforming of methane is a process in which hydrogen can be produced from methane in natural gas using high temperature steam. In a similar liquid reforming process liquid fuels such as ethanol are reacted with steam at high temperature to produce hydrogen near the point of end-use. Electrolysis uses electricity generated by wind, solar, geothermal, nuclear, or hydroelectric power to split water into hydrogen and oxygen. In gasification, coal or biomass is converted into gaseous components and then into synthesis gas, which is reacted with steam to produce hydrogen. Thermochemical water splitting uses high temperatures generated by solar concentrators or nuclear reactors to drive chemical reactions that split water to produce hydrogen. In photobiological process, microbes such as green algae consume water in the presence of sunlight producing hydrogen as the by-product. Similarly, photocatalytic and photoelectrochemical systems produce hydrogen from water using special semiconductors and energy from sunlight.

As shown in Fig. 3 natural gas reforming accounts for about 95% of the hydrogen produced today [2]. However, there is a limited supply of natural gas so hydrogen production from this source is not considered as a long-term option [7]. The total predicted US consumption of natural gas for the year 2030 is 26.1 Tcf (Trillion cubic feet), whereas the predicted production of natural gas is only 20.5 Tcf. Using solar energy for hydrogen production, such as via photobiological, photocatalytic, and photoelectrochemical processes, is an option for long-term hydrogen production. Nanotechnology is becoming increasingly significant in this field. The following sections describe the principle of solar hydrogen production as well as the role of nanotechnology in enhancing process efficiency.

Solar hydrogen production and the role of nanotechnology

Solar hydrogen represents a clean and abundant source of hydrogen [5, 8]. It is produced by driving water electrolysis with photoelectrochemical cells (Fig. 4), by direct photocatalytic splitting of water into hydrogen and oxygen

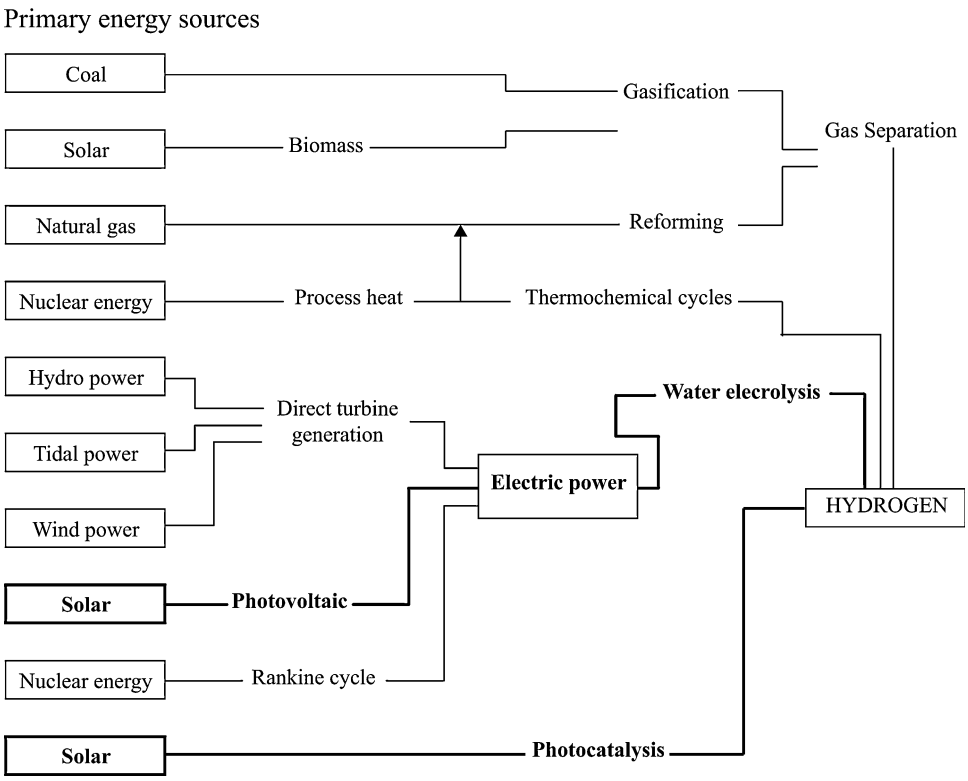

Fig. 2 Primary energy sources and their use in hydrogen production

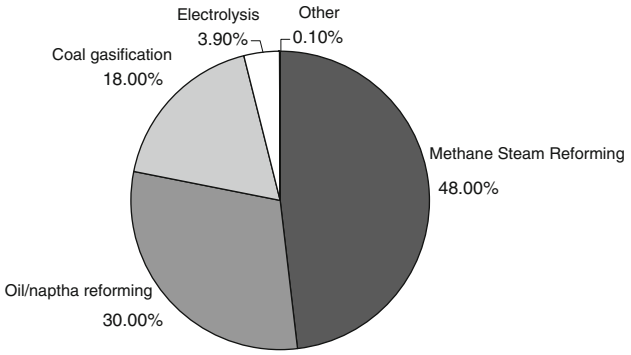

Fig. 3 Present distribution of primary energy sources for hydrogen production (data from [2])

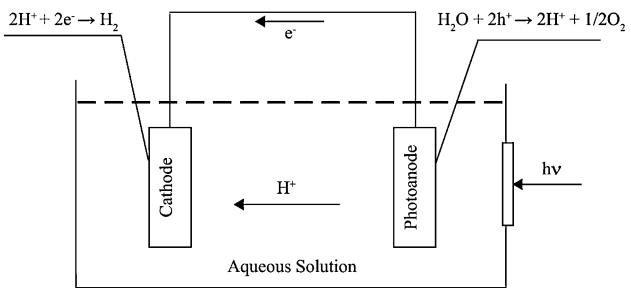

Fig. 4 Photoelectrochemical cell equipped with a single photoelectrode for water electrolysis

(Fig. 5), by photobiological water splitting or by solar thermal processes. Although solar to electric energy conversion is an established technology, current solar cells are too expensive for hydrogen generation. A cost reduction of a factor of $\sim$20 is required for widespread implementation of solar water splitting. An additional limitation is that most solar cell materials such as Si, CdTe, and GaAs are unstable in aqueous solutions. Semiconducting metal oxides such as TiO_2, ZnO, and Fe_2O_3 are cheaper and also more stable than conventional solar cell materials. Nanostructures of these cheaper and more abundant semiconductors exhibit novel properties that may make solar hydrogen production commercially viable. The following sections focus on the use of semiconductors and their nanostructures as photocatalysts/photoelectrodes for solar energy-induced water splitting for hydrogen production.

TiO_2 and its nanostructures for photoelectrochemical applications

TiO_2, with a band-gap energy of 3.0–3.2 eV, absorbs mainly in the UV region and to a lesser extent in the visible. Only 5% of the solar spectrum is UV in air mass (AM) 1.5:AM 1.5 corresponds to the solar energy received at the earth's surface when the sun is at 48.81° above the horizon [9, 10]. A band-gap energy of $\sim$1.7 eV is required for a semiconductor to efficiently absorb in the visible region. Nonetheless, TiO_2 is a widely used photocatalyst/photoanode for direct water

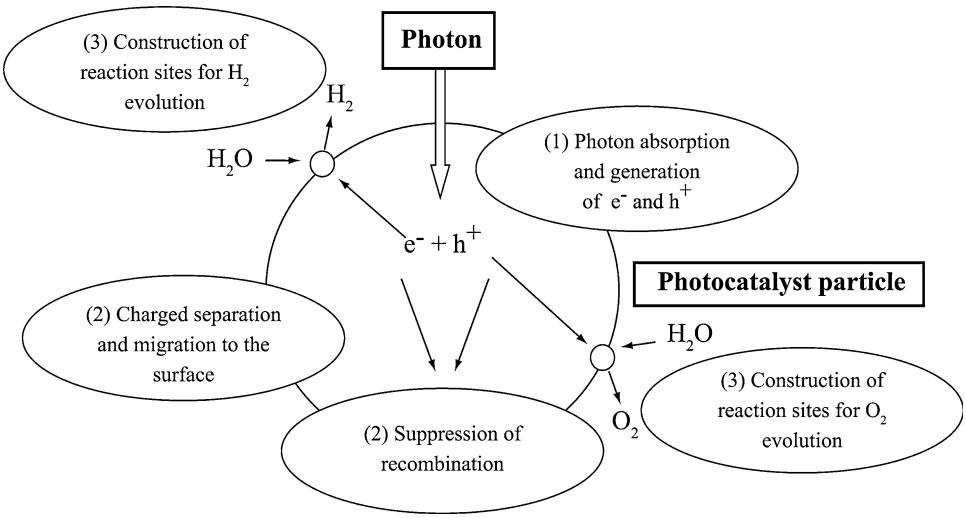

Fig. 5 Processes in a photocatalytic reaction (after: [13, 14])

splitting because it is stable, non-corrosive, environmentally friendly, abundant, and cost effective [8].

Photoelectrochemical decomposition of water and generation of hydrogen using TiO_2 was first reported by Fujishima and Honda [11]. An electrochemical cell was constructed in which a single crystal TiO_2 anode was connected with a Pt black cathode through an external load. When the TiO_2 was irradiated, oxygen formed at the electrode surface while hydrogen gas was formed on the Pt. A sequence of reactions that causes splitting of water without applying any external voltage was proposed [11]:

$$TiO_2 + 2h\nu = 2e^- + 2p^+ \text{ (excitation of } TiO_2 \text{ by light)}, \quad (1)$$

$$2p^+ + H_2O = \tfrac{1}{2}O_2 + 2H^+ \text{ (at the } TiO_2 \text{ anode)}, \quad (2)$$

$$2e^- + 2H^+ = H_2 \text{ (at the Pt cathode)}. \quad (3)$$

Since then, numerous studies have been conducted using various semiconducting metal oxides for photoelectrochemical and photocatalytic splitting of water for hydrogen generation [8, 12, 13]. This method is especially attractive because the two gases are separated immediately after water splitting.

The main processes in solar water splitting involve absorption of photons, charge separation and migration, and the surface chemical reactions [14]. The energy conversion efficiency from solar to hydrogen by TiO_2 photocatalytic water splitting is adversely affected by recombination of photogenerated electron hole pairs, fast backward reaction, and inability to utilize visible light [15]. In order to maximize water splitting efficiency of a TiO_2 photoanode, one would like a narrower band gap to capture more visible light, a high contact area with the electrolyte to increase the splitting of the electron hole pairs, and a thicker film to increase the total light absorption [16]. Nanostructured TiO_2 has the ability to enhance the surface adsorption as well as the photocatalytic reactions. It can also improve the ability to utilize visible light and hence improve the overall efficiency.

Qian et al. [17] synthesized three kinds of TiO_2 nanostructured thin films consisting of different sized nanoparticles, 4.5, 5, and 15 nm. The films were prepared by applying a colloidal suspension of nanoparticles onto a piece of indium tin oxide (ITO) coated glass. The films were dried at room temperature and then heated at 623 K for 30 min. It was shown that the smaller the particle size, the larger the photocurrent response. In a comparative study of thin film and TiO_2 nanowire electrodes, Khan and Sultana [18] observed a twofold increase in maximum photoconversion efficiency when a single layer thin film of TiO_2 was replaced by nanowires (Fig. 6). The nanowires were prepared by slowly adding drops of a TiO_2 sol to an alumina membrane (10 μm thick, 0.2 μm pore diameter, and $1.6 \times 10^9/cm^2$ pore density).

TiO_2 nanotubes have also been shown to harvest solar energy more effectively (show better photocurrent response) than planar foil photoanodes under the same illumination [16, 19, 20] as illustrated in Fig. 7. Xie [21] fabricated crystallized nanotubular TiO_2/Ti photoanodes as shown in Fig. 8. These showed better photocurrent response than their amorphous counterpart. A higher photocurrent indicates that photoinduced electrons transferred more efficiently from the anode to the cathode. The nanotubular channels may facilitate electron transfer. Figure 9 shows that the photocurrent density increases with aspect ratio in an ordered array of TiO_2 nanotubes [16]. With increase in tube length, the effective surface area in contact with the electrolyte increases. As a result, the charge transfer rate at the nanotube/electrolyte interface would be greater and could more than offset the adverse effects of bulk and surface recombination. Photon absorption also increases with aspect ratio. Thicker films of well crystallized ordered arrays of TiO_2 nanotubes

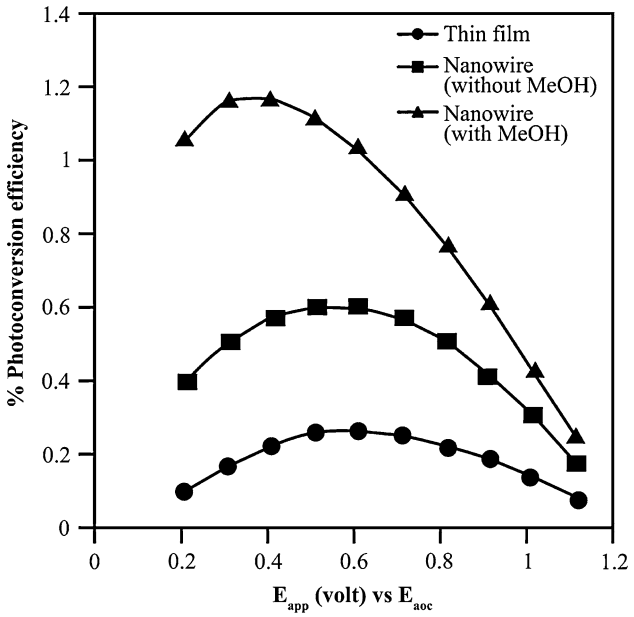

Fig. 6 Photoconversion efficiency as a function of applied potential for nanoparticulate TiO_2 thin film and nanowire with and without MeOH (data from: [18])

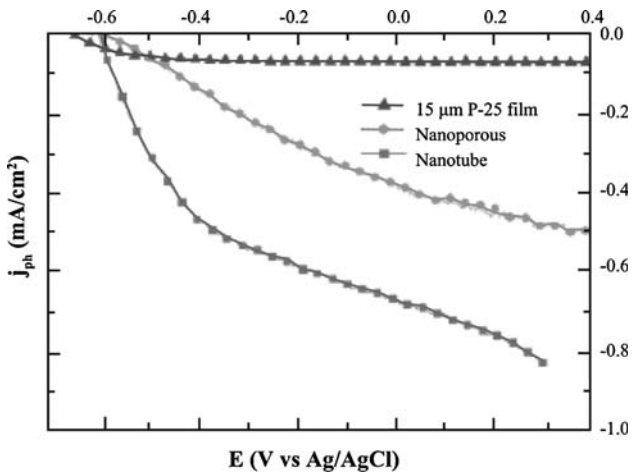

Fig. 7 Variation of photocurrent density with measured potential for 15 μm thick film of TiO_2 nanoparticles (P-25 from Degussa), nanoporous film and nanotube array (data from: [16])

appear to exhibit the best performance for solar water splitting.

Modification of TiO_2 nanotubes [16, 20, 22] and nanoparticulate thin films [23] with carbon has been reported to enhance photoactivity. Park et al. [16] prepared vertically grown carbon modified TiO_2 nanotubes with high aspect ratios. The modified $TiO_{2-x}C_x$ nanotubes were 3 μm long arrays and showed much higher photocurrent densities and more efficient water splitting under visible light than pure TiO_2 nanotube arrays. The total photocurrent was more than 20 times higher than that obtained with a nanoparticulate film under white light illumination [16].

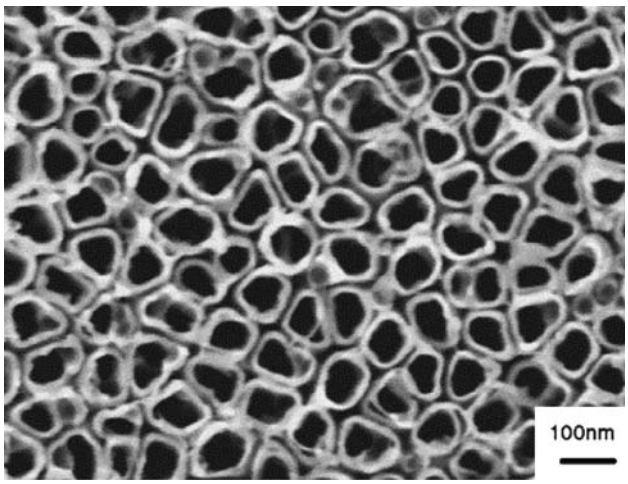

Fig. 8 SEM image showing nanotubular array of TiO_2 (reprinted from [21], copyright (2006) with permission from Elsevier)

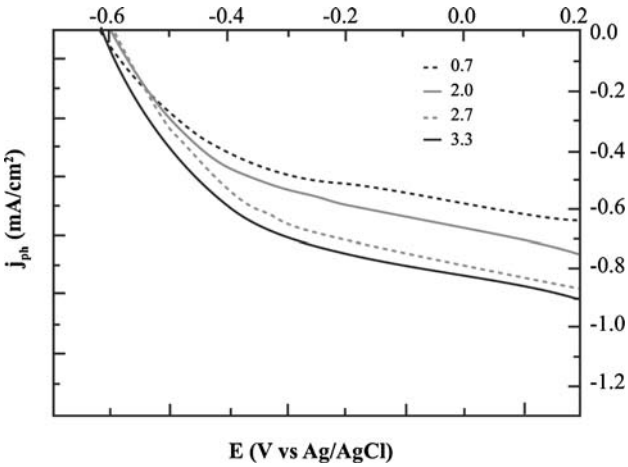

Fig. 9 Effect of TiO_2 nanotube length (μm) on photocurrent density (data from: [16])

Substitution of carbon for oxygen in TiO_2 reduced the band gap to 2.22 eV.

Xu et al. [20] synthesized carbon-modified TiO_2 nanotube arrays by anodization of Ti in a fluoride solution, subsequently annealed in air followed by natural gas flame oxidation. The carbon-doped TiO_2 nanotubes showed an eightfold increase in photocurrent density as compared to that of undoped TiO_2 thin films. Also, the utilization of solar energy extended into the IR region. The band gap of TiO_2 was reduced to 2.84 eV and an additional level was introduced 1.30 eV above the valence band. Misra et al. [22] prepared nanotubular arrays of TiO_2 and reported that annealing in a carbon-containing atmosphere enhanced photoactivity. The measured band gap was <2.4 eV. However, instead of just substituting for oxygen in the TiO_2 lattice, carbon deposited as a thin layer on the nanotube surface. Increasing the exposure time in

Table 1 Synthesis of nanotubular arrays of TiO_2 (with and without carbon doping)

References	Electrolyte	Bath temp (°C)	Anodization		Annealing		Carbon doping
			Time	Voltage (V)	Temp (°C)	Time (h)	
Macak et al. [24]	1 M H_2SO_4 + HF (0.15 wt.%)	2–20	2 h	20	Dried in nitrogen stream		
Mor et al. [25]	0.5 % HF + acetic acid (7:1)	5–50	–	10 and 20	500 in oxygen	6	–
Misra et al. [22]	(1) 0.5 M H_3PO_4 + 0.14 M NaF (pH-2)	24	50 min	20	350–500	1–6	Heated in acetylene + argon + hydrogen atmosphere in a CVD furnace
	(2) 0.5–1.0 M $NaNO_3$ + 0.14 M NaF (pH-3.8-5)		1–6 h				
Park et al. [16]	1 M $(NH_4)H_2PO_4$ + 0.5 wt.% NH_4F	–	–	15 (V increased from 0 to 15 at 1 V/s	450 in oxygen	1	Heating at temperature 500–800 °C under controlled CO gas flow
Xie [21]	0.15 M HF + 0.5 M H_3PO_4	–	40 min	20	500	2	–
Xu et al. [20]	0.1 M ammonium fluoride + 1 M ammonium hydrogen sulphate + 0.2 M triammonium citrate (pH-5)	–	20	20	500 in air	1	Heating in natural gas flame at 820 °C for 18 min

the carbonaceous atmosphere resulted in the growth of carbon nanostructures within the TiO_2 nanotubes.

Table 1 summarizes the synthesis methods for ordered arrays of undoped TiO_2 nanotubes and carbon-doped nanotubes. The properties of these arrays can be controlled by varying the processing conditions, e.g., the composition and pH of the anodizing solution. The thickness and length of the nanotubes varies with anodization temperature. Tube wall thickness and tube length increases by reducing the anodization bath temperature (Table 2) [25]. Mor et al. [25] also showed that the arrays prepared at lower temperatures exhibited better photocurrent density (Fig. 10).

Adsorption of Au nanoparticles ($\sim$10 nm) on the walls of TiO_2 nanotubes decreased the bias potential required for the enhanced photoactivity [22]. The Au nanoparticles were prepared by sputtering and decorated the brim of the nanotubes as shown in Fig. 11. In a study of photoelectrochemical behavior of nanoporous TiO_2 thin film electrodes modified with Au nanoparticles ($\sim$4 nm), Lana-Villareal and Gomez [26, 27] observed an increase both in photocurrent and photopotential that was attributed to efficient hole consumption at the Au particles. The Au

Table 2 Variation of nanotube length and wall thickness with anodization temperature (data from: [25])

Anodization temp (°C)	Wall thickness (nm)	Tube length (nm)
5	34	224
25	24	176
35	13.5	156
50	9	120

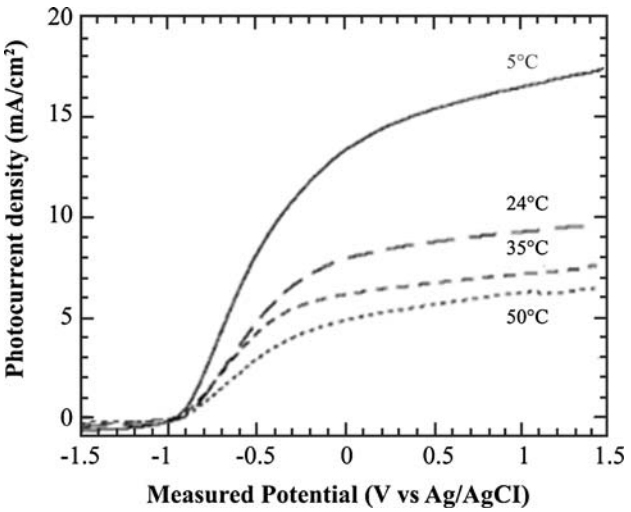

Fig. 10 Effect of anodization temperature on photocurrent density (data from: [25])

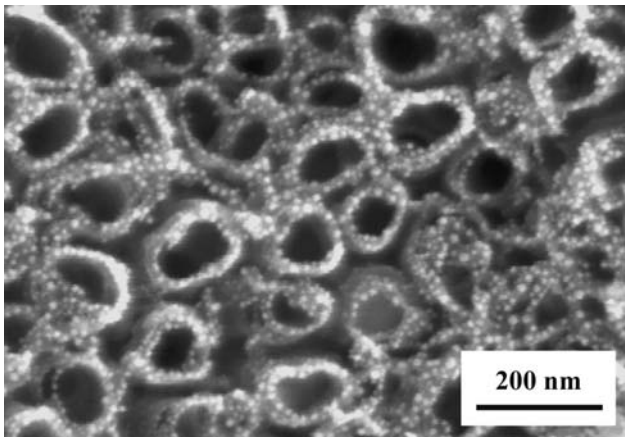

Fig. 11 SEM image showing gold nanoparticles decorating the brim of TiO_2 nanotubes (reprinted from [22], copyright (2006) with permission from SPIE and the authors)

particles were deposited simply by dipping the thin films in an aqueous colloidal dispersion.

The effect of Pt concentration on the production of hydrogen by a TiO_2 photocatalyst was investigated by Ikuma and Bessho [28]. The rate of hydrogen production was found to initially increase with the amount of Pt deposited, reach a maximum and then gradually decrease. Doping of TiO_2 with Nb also increased the solar to hydrogen conversion efficiency [29]. Coating TiO_2 nanotubes with WO_3 has been reported to enhance the visible spectrum absorption of the TiO_2 nanotube array, as well as their solar spectrum induced photocurrents [19] (Fig. 12). However, the reason for such an influence of WO_3 is not clear.

The use of nanostructures, particularly TiO_2 nanotubes, appears beneficial for enhancing solar to hydrogen conversion efficiency of TiO_2-based photoelectrochemical cells. Nanotubes of TiO_2 with high aspect ratio are capable of absorbing photons more efficiently and also increase the rate of charge transfer. Modifying these nanostructures with elements like carbon can reduce the band gap, thus improving visible light utilization. An ordered array of carbon modified TiO_2 nanotubes with high aspect ratio appear to be so far the best suited candidate for solar water splitting. Also as shown in Table 1, such ordered arrays can be conveniently synthesized by anodization of titanium sheets at temperatures close to room temperature and subsequent annealing. TiO_2 nanotube arrays with very high aspect ratios and length as large as 1 mm have been fabricated [30–32] by anodizing both sides of Ti foils in electrolytes containing NH_4F, H_2O, and ethylene glycol. Anodization for long times resulted in complete transformation of Ti to TiO_2 nanotubes.

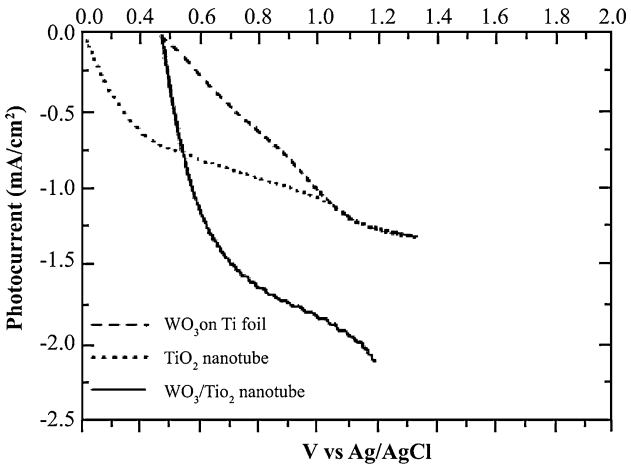

Fig. 12 Variation of photocurrent density versus applied potential for WO_3/Ti foil, TiO_2 nanotube arrays, and WO_3/TiO_2 nanotube nanocomposite (data from: [19])

Dye-sensitized photoelectrochemical cells

Nanocrystalline TiO_2 is used in dye-sensitized solar cells (DSSC), also known as 'Grätzel cells,' which are photoelectrochemical cells that use photosensitization of wide-band-gap mesoporous oxide semiconductors. Grätzel cells have a solar energy conversion efficiency >10% [33, 34]. An illustration of the operation of a DSSC is shown in Fig. 13. These cells consist of a layer ($\sim$15 μm) of TiO_2 nanocrystals ($\sim$20 nm diameter) coated with a dye and placed between two electrodes in an electrolyte-containing iodide ions or other redox mediator. The energy absorbed by the dye causes electron transfer from the dye molecules to the TiO_2, thereby oxidizing the dye. The electrons travel through the conducting glass electrode to the cathode through the external circuit and thus a current is generated. The iodide ions carry the electrons back to regenerate the dye.

The most successful charge transfer sensitizer employed so far in such cells, *cis*-dithiocyanatobis(2,2′-bipyridyl-4,4′-dicarboxylate)ruthenium(II) (together with its various

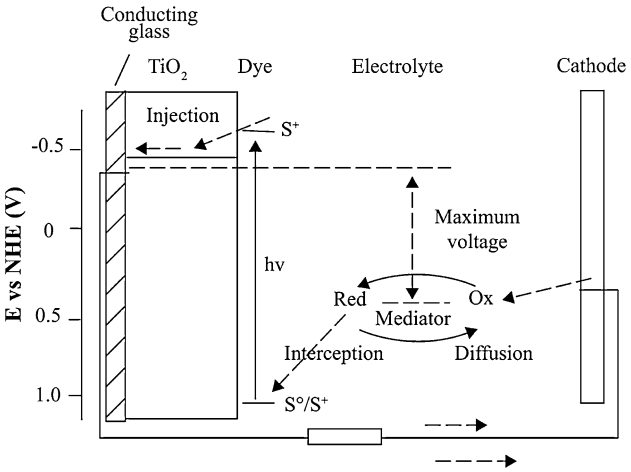

Fig. 13 Schematic showing operation of dye-sensitized electrochemical photovoltaic cell (after: [34])

protonated forms), yields conversion efficiencies of 10–11% under AM 1.5 [35, 36]. However, availability of these Ru dyes is limited and they are not environmentally friendly. Many efforts are being made to develop new organic dyes that are safer and derived from nature [36–38].The use of porphyrins as light harvesters on semiconductors is particularly attractive, given their primary role in photosynthesis and the relative ease with which a variety of covalent or non-covalent porphyrin arrays can be constructed [36, 37, and refs therein]. These naturally-derived dyes yield conversion efficiencies of 5–7% [37].

Improving efficiency involves absorption of the entire solar spectrum as well as improving the photocurrent response. Replacing the nanoporous particulate thin films with TiO_2 nanotubes [39] could be one method by which the photocurrent response might be significantly enhanced due to an increased rate of charge transfer. In order for photocatalysis-based applications to become commercially viable, it is critical to design low-cost methods that yield reproducible and easy-to-handle nanomaterials with high surface area and high porosity. The cost of these cells could be reduced by finding alternatives to organic dyes, e.g., with quantum dots (Q-dots).

Q-dots are semiconductor nanoparticles that exhibit physical and chemical properties that differ from bulk material as a result of quantum confinement of electrons [40]. The energy gap (and hence the absorption spectrum) of Q-dots can be tuned to energies higher than the bulk value by controlling the particle size. This property makes them attractive replacements for costly organic dyes [41–47]. CdS, CdSe, Bi_2S_3 are some examples of Q-dots that have been identified to be used to improve the photocurrent response.

Dye sensitization is also becoming important in photocatalytic hydrogen generation using non-TiO_2-based photocatalysts. Li et al. [48] reported photocatalytic water reduction for hydrogen generation using a multi-walled carbon nanotube (MWNT) based photocatalyst. They used an Eosin Y dye (bisodium salt—2′, 4′, 5′, 7′-tetrabromofluorescein) sensitized MWNT/Pt catalyst. The hydrogen generation rate reported by the authors was as high as 3.06 mmol/h g under visible light illumination. This rate is ~100 times higher than that observed by Ou et al. [49] for an MWNT–TiO_2/Ni composite photocatalyst (38.1 μmol/h g). This new catalyst could maintain ~70% of the initial activity after reaction for 100 h.

Other semiconducting photocatalysts/electrodes for solar hydrogen production

Many other metal oxides such as Fe_2O_3, WO_3, SnO_2, ZnO, TaO_3 have been investigated for potential application in the photocatalytic and/or photoelectrochemical splitting of water for hydrogen generation. Theoretically Fe_2O_3 is capable of utilizing a larger fraction of the solar spectrum compared to TiO_2 [50–52] because of its smaller band gap (~2.2 eV). Also, Fe_2O_3 is chemically stable over a broad pH range [53]. However, it suffers from high recombination losses. The short diffusion length of photoexcited charge carriers in Fe_2O_3 is one of the factors limiting the water splitting efficiency of iron oxide-based materials [52]. Present conversion efficiencies are a long way from the theoretical maximum [51]. Lindgren et al. [50] fabricated a Fe_2O_3 nanorod array with the aim of direct splitting of water. Despite the designed morphology, the rate of recombination was still high when an aqueous electrolyte was used. This was attributed mainly to bulk recombination and slow water oxidation kinetics at the interface. Recently, Glasscock et al. [51] reported fabrication of α-Fe_2O_3 nanostructured electrodes for photoelectrochemical water splitting. Thin films of Fe_2O_3 were deposited onto nanostructured substrates (ZnO nanowires and TiO_2 nanotubes) by filtered arc deposition. The one-dimensional nanostructures acted as conducting substrates [51, 52] and could overcome the problem of short diffusion length. However, detailed analysis of the photoelectrochemical properties of these nanostructures is pending.

Nanostructured thin films of WO_3 have been identified as photoanodes for solar water and sea water splitting as well as for photodegradation of industrial waste water containing organic chemicals [54]. The band gap of WO_3 is 2.5 eV and thus it absorbs in the blue part of the solar spectrum. It is one of the few semiconductors that are chemically inert and photostable (capable of maintaining its activity over a period of time) in acidic pH. Nakato et al. [55] fabricated a composite Si/ITO/WO_3 semiconductor electrode for photosplitting of water, where WO_3 was added to stabilize Si in aqueous solution. However, the anodic photocurrent density was found to be very low for efficient water splitting. Addition of methanol to water resulted in an increase in photocurrent. Methanol may have reduced the density of charge recombination centers on the WO_3 film. Development of metal oxide semiconductors with better photocurrent response is required to stabilize Si in aqueous solutions and achieve efficient water splitting.

Maeda et al. [56, 57] reported that solid solution of gallium and zinc oxynitride $(Ga_{1-x}Zn_x)(N_{1-x}O_x)$, impregnated with nanoparticles (10–20 nm) of a mixed oxide of rhodium and chromium, could be used as a photocatalyst for hydrogen production by solar water splitting. The photocatalyst did not show any degradation in activity after 35 h. The photocatalytic activity could be further enhanced by increasing the number of hydrogen evolution sites. Incorporating Pt or RuO_2 nanoparticles on the surface as suggested by Shangguan [14] could be a method of increasing the density of such sites. Ritterskamp et al. [58] reported the use of $TiSi_2$ as a catalyst for photocatalytic

water splitting based on its broadband absorption characteristics (band gap range is 3.4–1.5 eV). $TiSi_2$ is however unstable in water due to oxide formation. Suitable methods for surface passivation are required to improve stability.

Yamada et al. [59] fabricated CdS electrodes coated with TiO_2 nanosheets for photocatalytic oxidation of water. This was accomplished by exfoliating crystalline TiO_2 into individual colloidal sheets and their subsequent layer by layer deposition onto a CdS substrate [60]. The substrate was alternately dipped in colloidal suspension of nanosheet and a solution containing metal cations. CdS was selected based on its favorable band-gap energy of 2.4 eV. The goal of TiO_2 coating was to prevent corrosion of CdS and facilitate water oxidation. However, photocorrosion of CdS eletrodes could not be prevented, probably because the nanosheets were too thin. Furthermore, the TiO_2 nanosheets adversely affected the photocatalytic activity. This was attributed to charge recombination centers created by metal cations used during nanosheet deposition. Coating CdS electrodes with thicker films consisting of TiO_2 nanoparticles rather than nanosheets might be beneficial. These coatings could be made thick enough to prevent photocorrosion as well as minimize charge recombination centers.

Shangguan and colleagues [14, 61, 62] proposed nanostructural modification on the surface and in the interlayer of catalysts to enhance the activity for photocatalytic hydrogen production. Layered metal oxides such as $KTiNbO_5$, $K_2Ti_4O_9$, and $K_2Ti_{3.9}Nb_{0.1}O_9$ were prepared, which were then intercalated with CdS. The photoactivity of the intercalated catalysts was found to be better than pure CdS and a physical mixture of the oxide with CdS [61]. This was attributed to the incorporation of CdS nanoparticles between the oxide layers and the resultant heterojunction. It was suggested that incorporation of CdS nanoparticles in the interlayer could suppress particle growth and hence facilitate electron diffusion. Addition of hole scavengers such as S^{2-} to the solution also enhanced the photoactivity. Among the three layered catalysts, $CdS/K_2Ti_{3.9}Nb_{0.1}O_9$ showed the highest activity. The reduction in electron density due to substitution of Nb for partial Ti facilitated quick transfer of the electrons and suppressed charge recombination. Tian et al. [62] also prepared $K_4Ce_2M_{10}O_{30}$ (M = Ta, Nb), which is a metal oxide with a band gap of 1.8–2.3 eV. Figure 14 shows the crystal structure of this complex oxide in which three different types of tunnels, namely, triangular, square, and pentagonal, were created [62]. This structure was beneficial for the formation of "nests," which act as active sites for impregnation with nanoparticles. The catalyst, $K_4Ce_2M_{10}O_{30}$ (M = Ta, Nb), was loaded with Pt, RuO_2, and NiO_x. The NiO_x loaded catalyst showed relatively better performance for photocatalytic water splitting. Figure 15 shows the catalyst loaded with NiO_x [14].

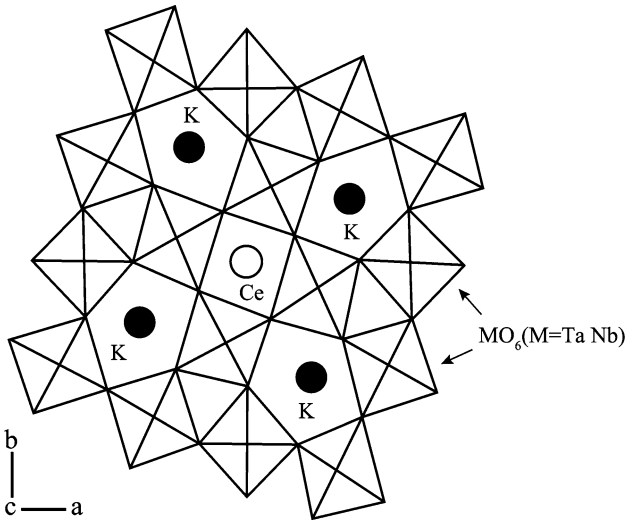

Fig. 14 Schematic crystal structure of $K_4Ce_2M_{10}O_{30}$ (M = Ta, Nb) (reprinted from [62], copyright (2006) with permission from Elsevier)

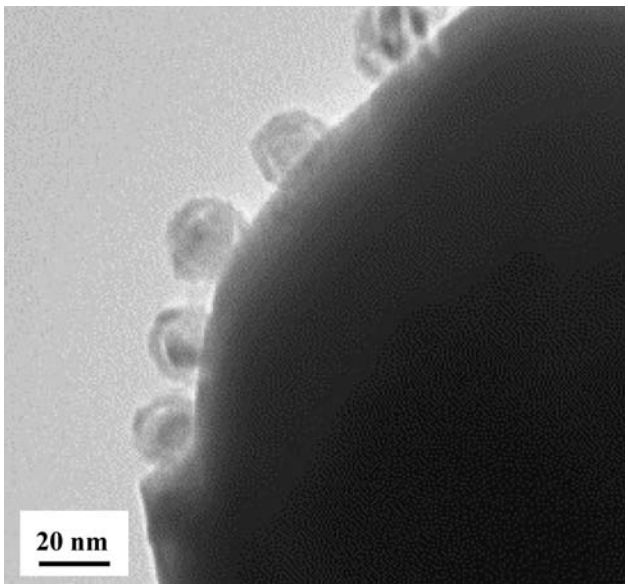

Fig. 15 TEM image of NiO_x anchoring on $K_4Ce_2Ta_{10}O_{30}$ (reprinted from [14], copyright (2007) with permission from Elsevier)

Solar hydrogen production by water splitting is becoming an attractive method of generating hydrogen owing to the abundance of both water and sunlight. The required minimum conversion efficiency is ~10%. Nanostructured photoanodes are critical for this technique to become commercially viable. This would include nanostructural modification of TiO_2. Research is also needed to develop suitable passivation techniques to prevent photocorrosion of conventional solar cell materials, which possess higher efficiencies but are unstable in aqueous solutions.

Hydrogen storage

Types of hydrogen storage systems and their requirements

Storage of hydrogen is required for stationary applications, such as residential heating and air conditioning and neighborhood electrical generation. It is critical for on-board automotive applications. The hydrogen storage systems for stationary applications can occupy a large area, employ multi-step charge/recharge cycles that operate at high pressures and temperatures, and compensate for slow kinetics by high capacity. On the other hand, the hydrogen storage systems required for transportation must operate with minimum weight and volume, supply enough hydrogen for a reasonable driving range, charge, and recharge near room temperature, and provide hydrogen at a rate fast enough for fuel cell locomotion of cars, trucks, and buses. A light-duty FCV must carry ~5–13 kg of hydrogen on-board (depending on the size and type of vehicle) to allow a driving range of more than 300 miles [6]. Table 3 shows specific performance targets for the transportation industry set by the US Department of Energy's Office of Energy Efficiency and Renewable Energy [4]. For on-board hydrogen storage, vehicles need compact (high volumetric capacity), safe, and affordable (~$4/kWh) containment. The material should be able to attain maximum storage capacity in the least amount of time (typically within 2–3 min) and at moderate temperatures.

Hydrogen has a very small specific volume as a gas. Hence, it requires high-pressure tanks, liquefaction, or some kind of physical or chemical bonding for solid state storage [63]. Compressed hydrogen is a potential hazard because it is highly flammable. Liquid hydrogen is a commercial product and is used as a rocket fuel with oxygen. Cryogenic liquid hydrogen (cooled to −253 °C) is stored in insulated cylinders at ambient pressure. Storing hydrogen in liquid form however has two major disadvantages [64, 65]:

- 30% energy loss due to refrigeration
- 1% boil-off rate

Because of the energy losses in liquefaction of hydrogen and the hazard potential of compressed hydrogen, it is desirable to store hydrogen in the solid state.

Table 3 DOE technical targets for on-board hydrogen storage systems (data from: [4])

Storage parameter	Units	Target year		
		2007	2010	2015
Usable, specific energy from H_2 (net useful energy/max system mass) (Gravimetric capacity)	kWh/kg (wt.% hydrogen)	1.5 (4.5 %)	2 (6 %)	3 (9%)
Usable energy density from H_2 (net useful energy/max system volume) (volumetric capacity)	kWh/L (kg H_2/L)	1.2 (0.036)	1.5 (0.045)	2.7 (0.081)
Storage system cost	$/kWh net ($/kg H_2)	6 (200)	4 (133)	2 (67)
Fuel Cost	$ per gallon gasoline equivalent at pump	3	1.5	1.5
Operating ambient temperature	°C	−20/50 (sun)	−30/50 (sun)	−40/60 (sun)
Cycle life (1/4 tank to full)	cycles	500	1000	1500
Cycle life variation	% of mean (min) at % confidence	N/A	90/90	99/90
Minimum and Maximum delivery temperature of H_2 from tank	°C	−20/85	−30/85	−40/85
Minimum full-flow rate	(g/s)/kW	0.02	0.02	0.02
Minimum delivery pressure of H_2 from tank; FC, fuel cell; I, ICE	Atm (abs)	8 FC 10 ICE	4 FC 35 ICE	3 FC 35 ICE
Maximum delivery pressure of H_2 from tank	Atm (abs)	100	100	100
Start time to full flow at 20 °C	Seconds	4	4	0.5
Start time to full flow at minimum ambient temperature	Seconds	8	8	4
System fill time for 5 kg hydrogen	Minutes	10	3	2.5
Transient response 10–90% and 90–0%	Seconds	1.75	0.75	0.5
Loss of usable hydrogen	(g/h)/kg H_2 stored	1	0.1	0.05
Permeation and leakage	scc/hour	Federal enclosed-area safety-standards		
Safety and toxicity		Meets or exceeds applicable standards		
Purity		98% (dry basis)		

Although, various solid state storage materials have been identified, none has been developed so far that can fulfill all the criteria given in Table 3. Based on the nature of absorption of hydrogen in the host material, solid state hydrogen storage materials can be divided into two categories:

- Atomic hydrogen storage materials or dissociative materials that store hydrogen mainly by dissociation of hydrogen molecules and atomic absorption, i.e., chemisorption
- Molecular hydrogen storage materials or non-dissociative materials that store hydrogen primarily by physisorption

The storage properties of some solid state hydrogen storage materials and their nanoscale modifications are discussed below.

Chemisorption

Metal hydrides

Hydrogen can be stored in the form of chemical compounds such as metal hydrides. During the formation of the metal hydride, hydrogen molecules are split and hydrogen atoms are inserted in spaces inside the metal lattice. Metals (M) react directly with hydrogen at a definite temperature and pressure according to the following reaction:

$$M + H_2 \leftrightarrow MH_2 + \Delta H. \quad (4)$$

Hydride formation is both exothermic and reversible. Hydrogen is released upon increasing the temperature and/or decreasing the pressure.

Hydrogen stored in the form of a hydride avoids limitations such as high pressure, large volume, low temperature, high evaporation losses, and safety risks that are encountered with gas or liquid storage. But the ability to use such a safe and efficient storage system will depend on identifying a metal with sufficient absorption capacity while operating in appropriate temperature ranges. Table 4 [3] lists several hydrides that have been studied as possible storage media along with their maximum gravimetric and volumetric capacities. The volumetric capacity of all hydrides is high. However, MgH_2 is the only one that is capable of meeting gravimetric storage capacity targets, rendering it particularly attractive for this application.

Table 4 Hydrides as hydrogen storage media (data from: [3])

Material	(Gravimetric capacity) Hydrogen content (kg/kg)	(Volumetric capacity) Hydrogen storage capacity (kg/L)
MgH_2	0.076	0.101
Mg_2NiH_4	0.0316	0.081
VH_2	0.0207	–
$FeTiH_{1.95}$	0.0175	0.096
$TiFe_{0.7}Mn_{0.2}H_{1.9}$	0.0172	0.090
$LaNi_5H_7$	0.0137	0.089
DOE target		
2007	0.045	0.036
2010	0.06	0.045
2015	0.09	0.081

Magnesium hydride and its nanostructures

Magnesium is considered a promising candidate for hydrogen storage because of its high nominal capacity of 7.6 wt.%. It should be noted that this storage capacity is defined for the material and not for the system. Also Mg is the seventh most abundant element, it is economical to extract, and non-toxic. However, stoichiometric MgH_2 is very stable ($\Delta H \sim 76$ kJ/mol) and suffers from very slow hydrogen absorption/desorption due to low diffusion constants. Hence, the practical application of Mg is limited because of sluggish kinetics even at elevated temperatures and the thermodynamic requirement of heating the material to temperatures close to 300 °C during dehydrogenation. The large enthalpy and exothermic nature of MgH_2 formation also results in evolution of heat during on-board recharging. The current cost of MgH_2 storage system is ~$8/kWh [4], which is twice as much as the 2010 target.

Structural and chemical modifications are essential to make Mg-based hydrides suitable for on-board hydrogen storage. Major aspects that should be considered and emphasized during synthesis and modification of Mg and Mg-based hydrides are:

- Enhancing the rate of hydrogen absorption and desorption
- Reducing reaction enthalpy so that desorption can take place at a lower temperature
- Improving cyclic hydrogenation/dehydrogenation (reversibility and durability for over 1,000 cycles)
- Enabling large scale production

Many methods such as catalyst addition (Ni, V, Nb, Fe, Ti, metal oxides, graphite, carbon nanotubes (CNTs)) [66–70], ball milling to decrease the crystallite and particle size [71–74], and mechanochemical methods [71, 72, 75–77] have been developed to improve the kinetics of hydrogen absorption and reduce the reaction enthalpy. Table 5 shows the effect of milling time on particle size, crystallite size, and desorption temperatures [71, 72]. The small size of nanostructured materials has a strong influence on the kinetics of hydrogen adsorption and dissociation due to the increase in the diffusion rate as well as the decrease in the required diffusion length.

Huot et al. [78] studied the effect of milling atmosphere on hydrogenation characteristics and composition of milled Mg–Ni compounds. For material milled under hydrogen,

Table 5 Effect of milling time on particle size, grain size and desorption temperature (data from: [71, 72])

Sample description	Phase present	Nanograin size of β MgH_2 (nm)	Mean particle size (μm)	Desorption onset temperature (°C)
As received MgH_2	β	67	35.8	406
MgH_2— milled 15 min	β	54	2.03	380
MgH_2—milled 1 h	β	60	0.96	356
MgH_2—milled 10 h	β, γ	14	0.47	345
MgH_2—milled 25 h	β, γ	13	1.30	372
MgH_2—milled 50 h	β, γ	13	1.18	365
MgH_2—milled 75 h	β, γ	11	0.84	352
MgH_2—milled 100 h	β, γ	3	0.6	342

the presence of Ni lowered the onset temperature of MgH_2 decomposition from 440 to 225 °C. By milling under argon, Mg_2Ni was formed, which slowed the decomposition kinetics of MgH_2 and raised the onset temperature to 263 °C. Zeng et al. [79] established a thermodynamic description of the Mg–Ni–H system and made an attempt to apply it to analyze the hydriding process of Mg–Ni alloys. The following reaction sequence for Mg–Ni alloys with <33% Ni was suggested:

$$\text{(i) } Mg_2Ni + H_2 = Mg_2NiH_{1-y}, \quad (5)$$

$$\text{(ii) } Mg + H_2 = MgH_2, \quad (6)$$

$$\text{(iii) } Mg_2NiH_{1-y} + H_2 = Mg_2NiH_{1-x}, \quad (7)$$

$$\text{(iv) } Mg_2NiH_{1-x} + H_2 = Mg_2NiH_4, \text{where } y > x \geq 0.7. \quad (8)$$

MgH_2 forms before Mg_2NiH_4 in these alloys because the chemical potential of hydrogen in MgH_2 is much more negative than in Mg_2NiH_4 [79].The calculated enthalpy changes for different steps of hydriding process of Mg_2Ni are shown in Table 6 [79].

Tessier and Akiba [80] also studied the influence Ni-doping on the dehydrogenation behavior of MgH_2. However, no significant change was observed probably because the amount of nickel used was very small (1 at.%). However, a MgH_2 composite with 1 mol% Ni prepared by milling for 15 min at 200 rpm desorbed a large amount of hydrogen (6.5 wt.%) in the temperature range 150–250 °C at a heating rate of 5 °C/min [81]. It has also been reported that ball milling of Mg and Mg_2Ni hydrides reduces the hydrogen desorption temperature by about 100 °C for MgH_2 and by 40 °C for Mg_2NiH_4 [74]. Unfortunately, the addition of Ni reduces the maximum hydrogen storage capacity of MgH_2.

Table 6 Calculated enthalpy change of hydriding process of Mg_2Ni (data from: [79])

Reaction	Temp (°C)	H (kJ/mol-H_2)
$Mg_2Ni + H_2 \rightarrow \gamma'\text{-}Mg_2NiH_{0.3}$	301	−34.7
$\gamma'\text{-}Mg_2NiH_{0.3} + H_2 \rightarrow Mg_2NiH_4$	301	−64.36
$Mg_2Ni + H_2 \rightarrow Mg_2NiH_4$	234	67.2

Reactive mechanical milling of Mg and 10 wt.% Co has been shown to result in improvement of hydrogen sorption properties [82]. The rate of formation of MgH_2 at 350 °C was fairly constant in the initial stages and decreased in the later stages (Fig. 16). This indicated that hydriding is a two-step process: nucleation of MgH_2 and diffusion through the hydride.

Liang et al. [83, 84] studied the effect of vanadium addition on hydrogen storage of mechanically milled MgH_2 and V powders. It was found that hydrogen desorption occurred at 200 °C under vacuum. Rapid re-absorption of hydrogen occurred even at room temperature. Figure 17 shows an image of mechanically milled MgH_2 + 5 at.% V nanocomposite. Each particle was made up of small crystallites. The enhanced kinetics was attributed to the catalytic effect of vanadium and the large Mg–V interface area. The V absorbed hydrogen and transferred it to the Mg–V interface, which provided active nucleation sites for MgH_2. The storage capacity was a function of temperature. It was a maximum of 5.6% at 200 °C decreasing to only 2% near room temperature.

The effect of nanostructures, surface catalysts, and alloying additions on the hydrogenation/dehydrogenation

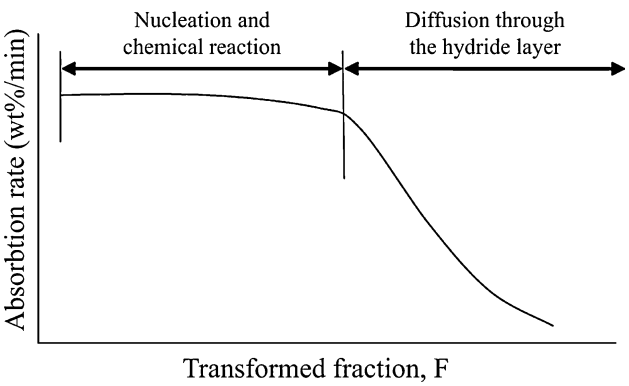

Fig. 16 Schematic illustration of the mechanism of hydride formation

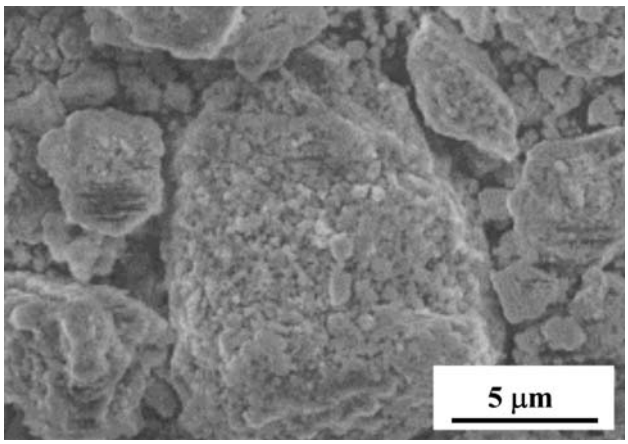

Fig. 17 SEM image of mechanically milled mixture of MgH_2 and 5 at.% V (reprinted from [83], copyright (1999) with permission from Elsevier)

properties of MgH_2 was also studied by Zaluska et al. [73]. They found that the combination of a nanocrystalline structure with surface modification improves the sorption kinetics. Magnesium powders were prepared with similar particle size (30–50 μm) but different crystallite sizes (1 μm to 30 nm). Hydrogen absorption rate as well as storage capacity were observed to increase with decreasing crystallite size (Fig. 18). Addition of a small amount (~1 wt.%) of catalyst (nanoparticles of Pd or Fe) improved the absorption kinetics as compared to the nanocrystalline powder without any catalyst. Catalyst addition offsets the negative effects of surface oxidation and eliminates the need for activation. The hydrogen

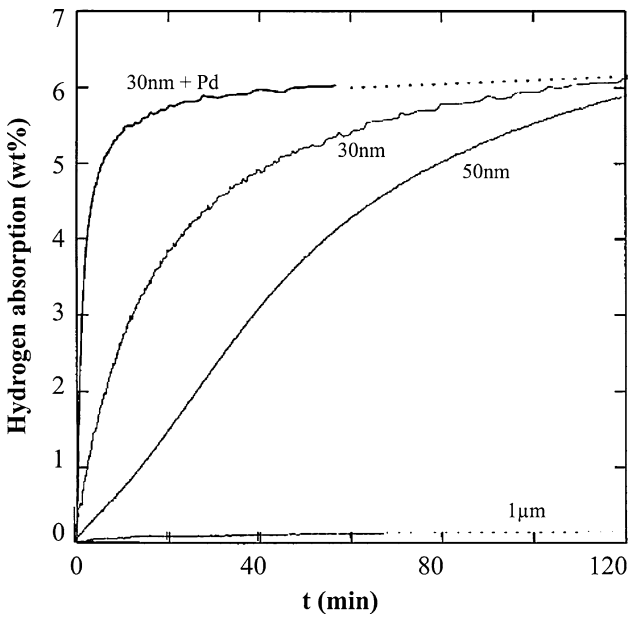

Fig. 18 Effect of grain size and Pd addition on hydrogen absorption of ball milled Mg powders (data from: [73])

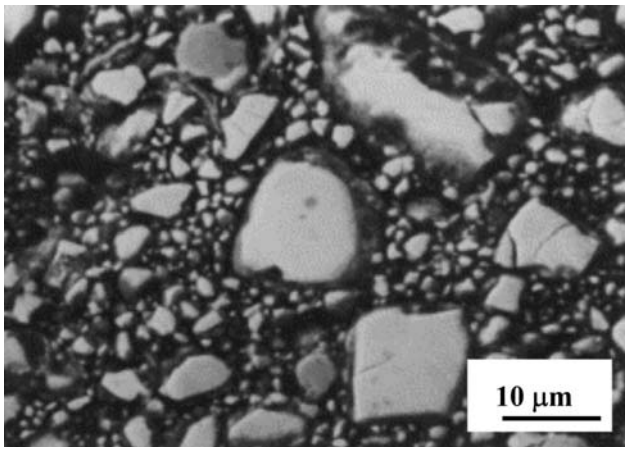

Fig. 19 SEM image showing MgH_2 (dark grey) around $La(Ni_{0.7}Fe_{0.3})_3$ particles (bright grey) (reprinted from [85], copyright (2000) with permission from Elsevier)

storage properties of materials produced by mechanical alloying of MgH_2 with several metallic additives such as $La(Ni_{0.7}Fe_{0.3})_5$, Pd_3Fe, and $(Fe_{0.8}Mn_{0.2})Ti$ were studied by Ruele et al. [85]. The crystallite size was found to vary from 25 to 200 nm depending on the milling time and the type of additive. These nanoscale composite materials exhibited enhanced desorption kinetics as well as reduced desorption temperature compared to pure ball milled MgH_2. As seen in Fig. 19, the additive particles were coated with thin layers of MgH_2 [85]. The improvement of desorption kinetics was attributed to the formation of a large MgH_2—additive interface and its resultant catalytic effect.

Wang et al. [86] hydrided Mg to nanostructured MgH_2 and γ-MgH_2 by direct ball milling along with a $ZrFe_{1.4}Cr_{0.6}$ catalyst and claimed that the hydrided phases possess improved desorption kinetics: 80% of the maximum capacity was desorbed in <15 min at 280 °C. The decomposition reaction of the hydrided phases was suggested to be nucleation controlled in the initial stages, and then the main reaction mechanism was growth controlled by the diffusion of hydrogen atoms [87]. Gennari et al. [88] also synthesized β- and γ-MgH_2 by reactive mechanical alloying (RMA) at room temperature under hydrogen atmosphere. The onset temperature of hydrogen desorption was observed to be 380 °C after 100 h of milling: γ-MgH_2 destabilized the β-MgH_2 phase, thus reducing desorption temperature.

In an attempt to assess the reality of lowering the hydrogen desorption temperature of Mg-based materials, Au [89] observed that addition of La, Ce, or $LaNi_5$ significantly reduces the absorption and desorption temperatures. However, at the same time, these alloying additions reduced storage capacity. Therefore an optimum value is necessary

to get a balance of the absorption/desorption kinetics and maximum storage capacity. The reduction in desorption temperature indicates thermodynamic destabilization of the hydride. The exact mechanism of the role of these alloying additions needs further investigation. The 3d transition metals like Sc and Ni have also been shown to have a catalytic effect on absorption kinetics [90].

Liu and Suda [91] reported that F-treatment of the surface of Mg_2Ni contributed to rapid initial activation at low temperatures. However, the hydriding ability of the material was very limited. Xie et al. [92] observed an increase in the absorption kinetics of hydrogen in MgH_2 nanoparticles (200 nm) doped with 5 wt.% of TiF_3 as compared to micrometer MgH_2 particles doped with TiF_3 (Fig. 20). The sample of nanoparticle $MgH_2 + 5$ wt.% TiF_3 absorbed 4.2 wt.% in 1 min at 27 °C. Absorption capacity increased to 4.6 and 5.0 wt.% at 100 and 200 °C, respectively. The absorption capacity was essentially independent of time beyond 1 min. The activation energy of dissociation of molecular hydrogen on pure Mg is very high, which means that the dissociation of molecular hydrogen and its absorption can take place only at high temperatures [93]. Also, it has been shown that when Ti is introduced, the activation barrier for hydrogen dissociation is reduced [94]. Therefore, hydrogen can be dissociated and hydrogenation can take place at lower temperatures in Mg doped with Ti. Doping of micrometer MgH_2 with TiF_3 also slightly reduced the desorption temperature and increased the rate of hydrogen desorption. However, reducing the particle size to the nanometer level did not have any significant influence on desorption rate. It was therefore suggested that desorption is not diffusion controlled. If desorption was diffusion controlled, reducing the particle size would have improved the kinetics.

Jin et al. [95] recently reported improved sorption kinetics by doping nanocrystalline MgH_2 with 1 mol% NbF_3. This material desorbed 6.3 wt.% of H_2 in 15 min and absorbed more than 90% of its initial hydrogen capacity in 5 min at 300 °C. The improvement in sorption kinetics was attributed to a very thin layer of Nb hydride formed at MgH_2 grain boundaries during ball milling, which suppress grain growth. The fast sorption kinetics was maintained even after 10 cycles.

In several studies it has been shown that CNTs have a positive effect on the absorption kinetics and hydrogen capacity as well as the cycling capability. Wu et al. [96, 97] incorporated single-walled carbon nanotubes (SWNT) by mechanically milling with MgH_2. A hydrogen capacity of >6.2 wt.% was reached in 10 min at 300 °C. The suggested mechanism for this improvement was the increased interfacial area (because of reduction in particle size during ball milling) and the increase in driving force for diffusion of hydrogen.

Yao and colleagues [98, 99] tried to develop Mg-based nanocomposites with nanoscale catalysts such as Fe and Ti that could enhance the kinetics of hydrogen absorption and desorption, and CNTs that could improve ambient hydrogen storage capacity. The results obtained for hydrogen absorption at 300 °C are summarized in Fig. 21. The enhancement in the absorption properties was attributed to CNTs serving as channels for hydrogen diffusion and also in facilitating ball milling by preventing agglomeration of MgH_2 particles. The grain size obtained by ball milling MgH_2–5 wt.% FeTi–5 wt.% CNT was ~11 nm. This material could desorb all of the stored hydrogen in ~80 min at 300 °C.

Enhanced kinetics was also reported in MgH_2 catalyzed by NbF_5 and SWNTs [100]. At 300 °C, the hydride was

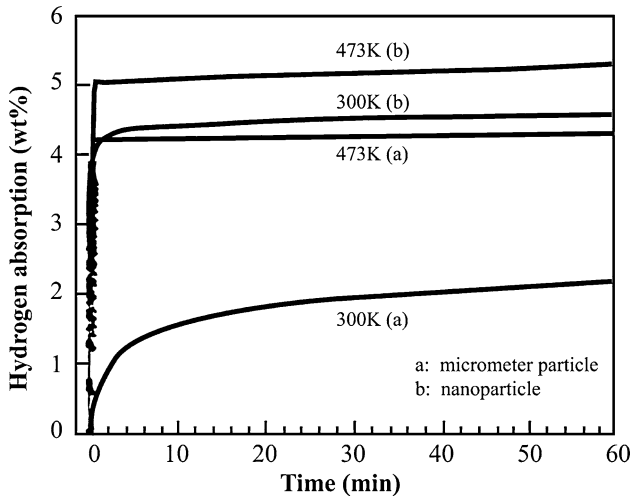

Fig. 20 Temperature dependence of hydrogen absorption in micrometer particles and nanoparticles of MgH_2 (data from: [92])

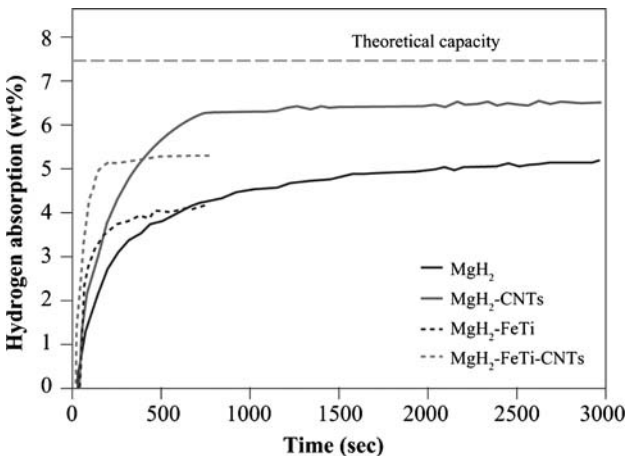

Fig. 21 Effect of FeTi and CNT on hydrogen absorption in MgH_2 (data from: [98])

able to absorb 6.3 wt.% within 30 s. Even at 100 °C the hydride was able to absorb 5.2 wt.% of hydrogen within 10 min. These results are of significance since the DOE target requires storage materials to absorb hydrogen at moderate temperatures. The cycling capacity was also enhanced in these samples. However, addition of SWNTs was observed to have a negative effect on desorption kinetics. The reason behind this degradation is still unclear. These samples were mechanically milled for only 2 h, which is probably not sufficient to produce nanoscale grains and enhance desorption properties. Milling for longer times, ~10 h, may be beneficial in this case.

The hydriding behavior of Mg and Mg–graphite based composites was studied by Imamura et al. [101–103]. The composites that showed the best results were those in which Mg particles, ~25 nm in diameter, were in intimate contact with graphite. Recently, Imamura et al. [104] prepared nanocomposites by ball milling graphite and Mg with organic additives such as benzene and cyclohexane. It was shown that the absorbed hydrogen existed in two states; one strongly associated with the carbon component and the other in a hydride. Ball milling resulted in the generation of large amounts of free carbon bonds in graphite, which acted as active sites to take up hydrogen. Huang et al. [105] reported that Mg milled with graphite under hydrogen exhibited improved absorption and desorption kinetics. They also reported that at 300 °C, a full hydrogen capacity of 6.2 wt.% could be reached within 2 min, and a complete release took place after 9 min. The hydrogen capacity and sorption kinetics in this case are very close to DOE targets, however the absorption and desorption temperature is still very high.

Metal oxides have been found to cause significant improvement in the hydrogen sorption kinetics of Mg-based hydrides. Huot et al. [106] showed that milling MgH_2 with 5 wt.% of Nb led to a material that could absorb and desorb hydrogen within a few minutes at 250 °C, suggesting a catalytic effect of Nb [106, 107]. Oelerich et al. [108, 109] and Barkhordarian et al. [110, 111] showed that additions of transition metal oxides with multiple valence states such as V_2O_5 and Nb_2O_5 led to a similar improvement in the sorption kinetics. This was attributed to the ability of Nb_2O_5 to split or recombine molecular hydrogen [110]. Hanada et al. [81] reported that desorption properties improve with milling time in the presence of Nb_2O_5 as the catalyst, which agrees very well with other studies. The MgH_2 composite with 1 mol% Nb_2O_5 prepared by milling for 20 h at 400 rpm desorbed 6.0 wt.% H_2 in the temperature range 200–250 °C at a heating rate of 5 °C/min. The Nb_2O_5-catalyzed composite also showed better cycling properties. However, Aguey-Zinsou et al. [112] were unable to confirm whether Nb_2O_5 acts as a catalyst for very small MgH_2 particles. It did facilitate MgH_2 particle size reduction when added in quantities ~17 wt.%. When milled for 200 h with Nb_2O_5, the average particle size of MgH_2 was ~300 nm. Whereas, milling of pure MgH_2 resulted in an average particle size that was three times larger. The Nb_2O_5 may prevent MgH_2 particle agglomeration during milling.

In an investigation of the influence of Sc_2O_3, TiO_2, V_2O_5, Cr_2O_3, Mn_2O_3, Fe_3O_4, CuO, Al_2O_3, and SiO_2 on the sorption behavior of nanocrystalline Mg-based systems Oelrich et al. [108] found that during absorption, the catalytic effect of the oxides were comparable. During desorption, the composite containing Fe_3O_4 showed the fastest kinetics followed by V_2O_5, Mn_2O_3, Cr_2O_3, and then TiO_2. Only small amounts (~0.2 mol%) of the catalysts was found to be sufficient to provide enhanced sorption kinetics. The catalytic effect was attributed to the ability of metal atoms to adopt different electronic states. Li et al. [113] proposed, by kinetic analysis of MgH_2 and MgH_2–Cr_2O_3 nanocomposites, that the rate controlling step during hydrogenation is the diffusion of hydrogen through the hydride.

Liu and Lei [114] studied the hydriding behavior of a nanocrystalline composite of Mg–3 wt.%Ni–2 wt.%MnO_2. The particle size of Mg was 75–170 μm and that of Ni and MnO_2 was 20–50 nm. In 50 s, 6.4 wt.% of hydrogen was absorbed at 200 °C. Almost the same amount of hydrogen was desorbed in ~300 s in the temperature range 285–310 °C under a hydrogen pressure of 1 bar. The composite also had better cyclic hydrogen properties. However, the absorption and desorption times increased with increase in the number of cycles. This behavior was attributed to the formation of MgO during the cycling process, which impedes contact of the catalyst with MgH_2.

Milling of Mg_2NiH_4 with platinum group metals (PGM) has been reported to decrease the desorption temperature [115]. The onset temperature of desorption was reduced to 120 °C by addition of 1 wt.% Pd-black. An even lower onset temperature of hydrogen desorption of 80 °C was observed when using 1 wt.% Ru. These low desorption temperatures were attributed to the combined effect of Ni and PGMs. The nanoscale structure and the hydrogen storage properties of Pd-capped Mg thin films were also studied [116]. The hydrogen sorption temperatures decreased from 397 to 202 °C by capping the Mg films with a 100 nm Pd layer, which plays a key role in enhancing the rate-limiting process of dissociating the hydrogen molecules at the sample surface. Cycling experiments showed that a clear reduction in hydrogen content occurred within only a few cycles due to partial delamination of the Pd layer. This clearly limits practical applications of such films. Moreover, thin film analysis cannot be directly translated to practical situations where large scale hydrogen storage is required. Magnesium films

(2 μm thick) with crystallite size of ~50 nm were fully hydrogenated to MgH_2 at 177 °C in 15 min and all of the hydrogen was desorbed at 257 °C [117]. The lower absorption and desorption temperatures were partly attributed to a larger fraction of grain boundaries in the finer grain sized films. Table 7 summarizes the hydrogen storage properties of some selected Mg-based hydrides.

As described above, numerous efforts have been and are being made to improve hydrogen storage properties of nanostructured Mg and Mg-based hydrides. However, more comprehensive studies are required to combine the positive impact of all modifications. Mechanical alloying of Mg or MgH_2 with transition metals results in enhancement of sorption kinetics and hydrogen capacity. However, it is not certain whether this enhancement is an effect of grain size reduction, a catalytic effect or some combined effect. It has been recently suggested that nanoparticle sizes in the single digits are required to obtain any significant enhancement in sorption kinetics [118, 119]. At present, the smallest particle size that has been observed is either in the tens or even hundreds of nanometers. In some cases, the hydrogen capacity has been found to decrease when the grain/particle size was reduced in an attempt to improve the sorption kinetics. A more meticulous investigation is required for delineating the influence of these factors and to optimize the grain size and alloying additions. Thermodynamic analyses of alloying additions are also essential for understanding and precisely predicting the effect of these additions.

Surface impregnation of MgH_2 with metal particles also results in enhanced sorption kinetics. These metal particles dissociate molecular hydrogen and the atoms then penetrate into the substrate. Addition of graphite and metal oxides such as Nb_2O_5 facilitates the milling process. Small amounts of these could be added during mechanical alloying to further improve hydrogen sorption kinetics. CNTs have been found to be beneficial in enhancing hydrogen absorption. Apart from facilitating the milling process, carbon nanostructures could be useful in storing a fraction of absorbed hydrogen by physisorption and improve the storage capacity at moderate temperature. Once all of the above issues are addressed, it may be possible to design a material based on MgH_2 for on-board hydrogen storage that might be able to absorb hydrogen at reasonable rates and moderate temperatures and maintain its storage capacity.

Synthesis and large scale production

Nanoscale hydrides can be prepared via two processes:

- Mechanically milling the metal in hydrogen or RMA
- Mechanically milling the hydride

Mechanical milling ensures uniform dispersion of alloying additions and nano-catalysts. Holtz and Imam [120] compared three different methods of synthesizing nanostructured Mg–Ni hydride:

- Ball milling
- Physical vapor deposition with inert gas condensation
- Pulverization with hydrogenation/dehydrogenation cycling of thin films

They found that the most efficient method is ball milling in terms of process yield and hydrogenation behavior.

Metal hydrides and complex metal hydrides have been synthesized by RMA [121]. For example, Bobet et al. [82, 122–124] synthesized MgH_2 via RMA at room temperature and studied the influence of addition of 3d-metals on the synthesis. It was observed that addition of 10 wt.% Co as a catalyst increased the yield of MgH_2 to 71% after 10 h of milling. On the other hand, milling for only 2 h increased hydrogen absorption kinetics at 350 °C. It is therefore essential to establish a critical milling time that would balance product yield and hydrogen absorption kinetics. Huot et al. [125] showed that a complete transformation from Mg to MgH_2 could be achieved in 1 h by milling at 300 °C under hydrogen pressure of 4 bar in the presence of graphite. Figure 22a, b shows the absorption and desorption behavior of MgH_2 synthesized by ball milling Mg and graphite under 4 bar of hydrogen at 390 °C for 5 h. The dehydrogenation kinetics of the synthesized sample was almost an order of magnitude faster than that of the commercial MgH_2. The hydrogenation kinetics of the synthesized sample was also better than the commercial MgH_2.

Another method of synthesizing Mg-based hydrides is hydriding combustion synthesis (HCS). The advantages of HCS are short process time, lower energy requirement, and high product purity [126]. It was shown that the product Mg_2NiH_4 produced by HCS has better hydrogen storage properties in comparison with commercially available ingot metallurgy product of Mg_2Ni [127]. However, the hydrogen storage properties reported by the authors are still a long way from DOE targets.

For practical applications, it may be advantageous to synthesize the hydrides directly in order to reduce or eliminate the need for an activation process. Reactive milling has been used by several researchers, both at room temperature and elevated temperatures, to directly synthesize Mg-based hydrides [77 and references therein]. Another positive aspect of this process is that it can be easily scaled up for commercial production. Vibration tube mills are an option for the production. These are available up to tonnage quantities, such as those used for mineral processing, and can operate in continuous mode [128]. It should be noted that hydride formation in nearly all metal systems involves a volume change of 15–25% and this

Table 7 Hydrogen absorption/desorption properties of Mg-based hydrides

References	Material	Particle size/grain size	Temp (°C)	Pressure (MPa)	Kinetics (min)	Cyclic properties	Capacity (wt.%)
Aguey-Zinsou et al. [112]	$MgH_2 + Nb_2O_5$	10–50 nm	$T_{abs} = 300$	$P_{abs} = 1$ MPa	2	–	6
			$T_{des} = 300$	$P_{des} = 0.1$ MPa	4–5		
Barkhordarian et al. [110]	MgH_2 —0.05–0.5 mol% Nb_2O_5	–	300	$P_{abs} = 0.84$ MPa	$t_{abs} = 1$	–	7
			300	P_{des} = vacuum	$t_{des} = 1.5$		
			250		$t_{abs} = 1$		6
			250		$t_{des} = 8.3$		
Hanada et al. [81]	MgH_2 – 2 mol%Ni	–	$T_{des} = 150$–250	–	–	2 cycles—not stable	6.5
	MgH_2 – 1 mol%Nb_2O_5		$T_{des} = 200$–250				6
Huot et al. [78]	Mg – 20 wt.%Ni	30 – 200 μm	$T_{onset} = 225.4$	–	–	–	–
Huot et al. [106]	MgH_2 – 5 at.%Nb	8–11 nm	–	–	–	–	–
Huang et al. [105]	$MgH_2 + G$	–	$T_{abs} = 300$	$P_{abs} = 2$ MPa	2	–	6.5
			$T_{des} = 350$	$P_{des} = 0.05$ MPa	9		
Imamura and Sakasai [103]	Mg – 5wt.%(Pd/G)	25 nm	–	–	–	–	–
Liang et al. [83]	MgH_2 – 5at%V	–	$T_{abs} = 200$	1 MPa	<1	–	5.5
			$T_{des} = 300$	0.015 MPa	4–5		
Liu et al. [114]	Mg – 3 wt.%Ni – 2 wt.%MnO_2	Mg – 75–170 μm	$T_{abs} = 200$	0.1 MPa	$t_{abs} = 1$	60 cycles—stable	6.5
		Ni and MnO_2 – 20–50 nm	$T_{des} = 285$–310		$t_{des} = 5$		
Au [89]	Mg – 20 wt.% $LaNi_5$	Amorphous	300	$P_{abs} = 3$ MPa	$t_{abs} = 7$–8	–	4.2
	Mg – 50 wt.% Ni	12 nm	300	P_{des} = vacuum	$t_{abs} = 5$		5.5
Reule et al. [85]	MgH_2 – 50 wt.%$La(Ni_{0.7}Fe_{0.3})$	P.S = 5 μm	–	–	–	–	–
		C.S = 25 nm					
	MgH_2 – 50 wt.%Pd_3Fe	P.S = 10 μm					
		C.S = 20 nm					
	MgH_2 – 50 wt.% Si	–					
Wang et al. [86]	MgH_2 – 40 wt.% $ZrFe_{1.4}Cr_{0.6}$	5–15 nm	$T_{des} = 280$	–	15–20	–	–
Wu et al. [97]	MgH_2 – 5 at.%SWNT	–	$T_{abs} = 300$	2 MPa	10	–	6.2
Yao et al. [98]	MgH_2 – 5 wt.%(2Fe + Ti)	13.9 nm	300	$P_{abs} = 2$ MPa	$t_{abs} = 10$	–	4.5
	MgH_2 – 5 wt.%FeTi – CNT	11.3 nm	300		$t_{abs} = 1$–2		5.5
Zaluska et al. [73]	Mg + Pd	30 nm	–	–	$t_{abs} = 20$	–	6

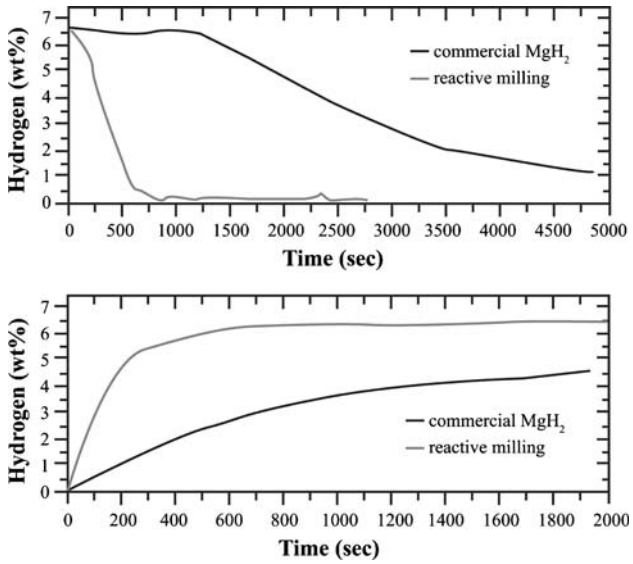

Fig. 22 Hydrogen absorption and desorption kinetics of commercial MgH_2 and Mg + graphite mixture (data from: [125])

must be taken into account while designing the storage container.

Physisorption

Metal organic frameworks

Metal organic frameworks (MOFs) are networks of transition metal atoms bridged by organic ligands that have been proposed as structured nanoporous materials for hydrogen storage [129–134]. Sometimes called crystal sponges, MOFs are essentially scaffolds made up of linked rods—the structure that makes for maximum surface area. MOFs provide systems with large overall pore volumes and surface areas, adjustable pore sizes, and tunable framework–adsorbate interaction by ligand functionalization and metal choice. The most striking feature of MOFs is the total accessible bulk volume. Hydrogen can be inserted and then removed reversibly without any change in the storage medium, unlike chemical bonding of hydrogen in metal hydrides. Of all available porous materials, MOFs show the highest surface area and therefore highest gravimetric uptake. However, the heat of adsorption of hydrogen on current MOFs is still quite low, typically 4–10 kJ/mol, which makes adsorption of any significant amount of hydrogen possible only at low temperatures (<100 K).

Investigation of hydrogen storage in MOFs was first reported by Rossi et al. [135] in 2003. They found that MOF-5 (a cubic three-dimensional extended porous structure with a composition Zn_4O(1,4-benzenedicarboxylate)$_3$; also known as isoreticular MOF-1 (IRMOF-1) could adsorb 4.5 wt.% of hydrogen at 77 K and 1 wt.% at room temperature. However, even at 20 bar pressure the MOF remained undersaturated with H_2 at room temperature. Room temperature adsorption requires much higher pressures. Since then, a number of experimental and computational works have been published. Figure 23 shows the structure of different IRMOFs (having the same underlying topology) that are constructed by linking ZnO clusters with linear carboxylates. MOF-177 is formed by linking the same clusters with a trigonal carboxylate [136]. Table 8 lists the types of MOFs reported to date, along with their specific surface area and hydrogen capacity.

Hirscher and Panella [137] reported that MOF-5 with specific surface area of 1,014 m^2/g showed a storage capacity of 0.2 and 1.6 wt.% at room temperature and 77 K, respectively. Subsequently, Panella et al. [138] reported that at high pressures and 77 K, MOF-5 was capable of adsorbing 5.1 wt.% hydrogen. The smaller hydrogen uptake values in the previous reference were attributed to the smaller specific surface area. They also found that another MOF, Cu_3(benzene-1,3,5-tricarboxylate)$_2$, or $Cu_3(BTC)_2$, adsorbed 3.6 wt.% at 77 K. However, at lower pressures $Cu_3(BTC)_2$ was able to adsorb more hydrogen as compared

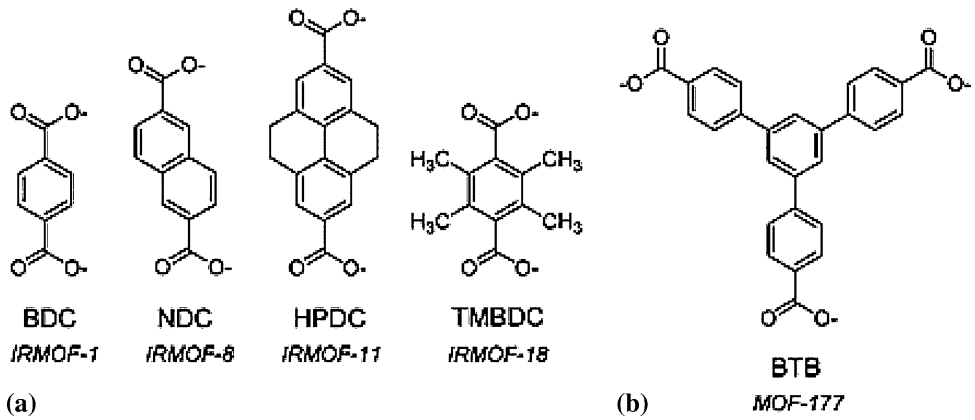

Fig. 23 Schematic illustration of the structures of (**a**) isoreticular MOFs and (**b**) MOF-177 (reprinted from [136] with permission from American Chemical Society)

Table 8 Hydrogen adsorption capacity of different MOFs along with their specific surface area

References	Type of MOF	SSA (m^2/g)	H_2 Capacity (wt.%)	Conditions (temp/pressure)
Furukawa et al. [150]	MOF–177	–	7.5	77 K/70 bar
Han et al. [148]	Mg-MOF-C30	–	8.08	77 K/ 20 bar
	Zn-MOF-C30	–	6.47	77 K/ 20 bar
	Be-MOF-C30	–	7.61	77 K/ 20 bar
Hirscher and Panella [137]	MOF–5	1014	1.6	77 K/ ~ 10–20 bar (saturation)
			0.2	RT/ 65 bar
Kraweic et al. [147]	$Cu_3(BTC)_2$	1,239 (BET)	2.18	77 K/ 1 bar
	IRMOF-8	890 (BET)	1.45	77 K/ 1 bar
Li and Yang [142]	MOF–5 (pure)	–	1.28	77 K/ 1 bar
	IRMOF-8 (pure)	–	1.48	77 K/ 1 bar
	MOF-5 (pure)	–	0.4	298/100 bar
	MOF-5 (physically mixed with 10 wt.% Pt/AC)	–	1.32	298/100 bar
	IRMOF-8 (pure)	–	~0.5	298/100 bar
	IRMOF-8 (physically mixed with 10 wt.% Pt/AC)	–	1.8	298/100 bar
Li and Yang [143]	IRMOF-8 (pure)	–	0.5	298/100 bar
	IRMOF-8(modified by Pt/AC bridges)		4.0	298/100 bar
Panella et al. [138]	MOF-5	3,840 (2296—BET)	5.1	77 K/saturation pressure
	$Cu_3(BTC)_2$	1,958 (1154—BET)	3.6	77 K/saturation pressure
Rossi et al. [135]	MOF-5	–	4.5	78 K/0.75 bar
			1.0	298 K/20 bar
Rowsell et al. [136]	IRMOF-1	3,362	1.32	77 K
	IRMOF-8	1,466	1.5	
	IRMOF-11	1,911	1.6	
	IRMOF-18	1,501	0.89	
	MOF-177	4,526	1.25	
Surble et al. [145]	MIL-102	–	1.0	77 K/35 bar
Wong-Foy et al. [149]	IRMOF-1	4,170	5.2	77 K/ ~ 50 bar
	IRMOF-6	3,300	4.8	77 K/ ~ 50 bar
	IRMOF-11	2,340	3.5	77 K/34 bar
	IRMOF-20	4,590	6.7	77 K/ ~ 70–80 bar
	MOF-177	5,640	7.5	77 K/ ~ 70–80 bar
	MOF-74	1,070	2.3	77 K/26 bar
	HKUST-1	2,280	3.2	77 K/ ~ 75 bar

to MOF-5 indicating higher interaction energy between hydrogen and adsorbent.

A computational study of MOF-5 found that the metal oxide cluster was primarily responsible for the adsorption while the organic linker played only a secondary role [139]. At low temperatures and high concentration, H_2 molecules form interlinked high-symmetry nanoclusters with intermolecular distances as small as 0.3 nm. Theoretically, hydrogen uptake as high as 11 wt.% is possible. In addition, MOFs can be used as templates to create artificial interlinked hydrogen nanocages. In a computational study of MOF-505 (Cu_2(3,3′,5,5′-biphenyltetracarboxylic group)), Yang and Zhong [140] showed that open metal sites of the metal oxygen clusters are preferential adsorption sites for hydrogen. Including such sites in the framework may have a favorable impact on the hydrogen sorption capacity. In a further theoretical investigation of the relationship between the molecular structures of MOFs and their hydrogen uptake,

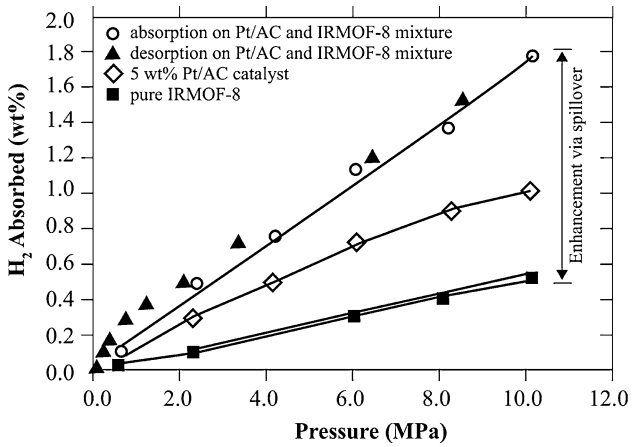

Fig. 24 High pressure hydrogen isotherms at 298 K for IRMOF-8 (data from: [142])

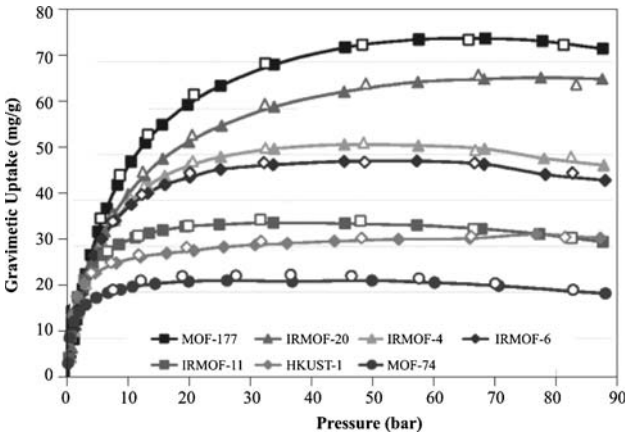

Fig. 25 High pressure hydrogen isotherms at 77 K for MOFs representing surface excess adsorption (data from: [149])

Kim et al. [141] showed that for structurally similar MOFs, functionalization of aromatic organic linkers could induce noticeable polarization effects on the framework surface. This would increase the interaction between hydrogen and framework.

Li and Yang [142] reported hydrogen uptakes of 1.28 wt.% for MOF-5 and 1.48 wt.% for IRMOF-8 at 77 K and 1.01 bar. The materials did not show saturation at such low pressures. The maximum uptake may increase with increase in pressure. Platinum supported on activated carbon (Pt/AC) catalyst was added by grinding the MOFs and the catalyst for 1 h with mortar and pestle, which increased the room temperature hydrogen adsorption by a factor of 3 (Fig. 24). This enhancement was attributed to spillover in which hydrogen is first adsorbed by the metal atom, then diffuses and becomes physisorbed. In another study, the same authors reported a reversible hydrogen capacity of 4 wt.% (~8 times pure IRMOF-8) at 298 K and 100 bar pressure for Pt/AC modified IRMOF-8 where primary and secondary spillover was facilitated by carbon bridges [143]. This phenomenon is also considered important for physisorption of hydrogen in CNTs and will be discussed in detail in the following sections.

Three Cu–MOFs were reported by Lin et al. [144] with the maximum hydrogen uptake of 7.01 wt.% at 78 K and 20 bar. A chromium (III) naphthalene tetracarboxylate MOF, $Cr^{III}{}_3O(H_2O)_2F\{C_{10}H_4(CO_2)_4\}_{1.5} \cdot 6H_2O$, was reported to exhibit a hydrogen storage capacity of 1 wt.% at 77 K and 35 bar [145]. The lower value of hydrogen uptake was attributed to the small free volume of ~26%. MOFs in general have a free volume in excess of 90%.

Liu et al. [146] studied two In-based MOFs and reported storage capacities up to 2.61% at 78 K and 1.22 bar. Increase in adsorption pressure may result in further improvement in storage capacity. Krawiec et al. [147] synthesized a nanoporous $Cu_3(BTC)_2$ MOF and reported a gravimetric capacity of 2.18 wt.% at 77 K and 1 bar. Han et al. [148] have very recently reported that replacing Zn with lighter metals like Be or Mg improved the hydrogen capacity at 77 K and 20 bar to 8.08 and 7.61 wt.%, respectively: three times higher than the performance of CNTs and porous carbon materials.

Rowsell et al. [136] reported hydrogen uptake measurements on five different MOF materials and found that IRMOF-11 showed largest hydrogen uptake (1.62 wt.%) at 77 K and 1.01 bar. Figure 25 shows results of a detailed investigation of hydrogen adsorption properties in seven different MOFs conducted by Wong-Foy et al. [149]. The H_2 uptake for MOF-177 and IRMOF-20 was 7.5 and 6.7 wt.%, respectively: saturation was reached between 70 and 80 bar for both MOFs. These values more than satisfy current gravimetric on-board storage requirements. However, volumetric capacities (~30 g/L) are ~75% of the DOE target of 45 g/L. Furukawa et al. [150] calculated the absolute adsorbed amount of H_2 in MOFs:

$$N_{\text{abs}} = N_{\text{ex}} + \rho_{\text{bulk}} V_{\text{pore}}, \tag{9}$$

where N_{abs} is the absolute adsorbed amount, N_{ex} is the surface excess amount, ρ_{bulk} is the bulk density of H_2, and V_{pore} is the pore volume. Experimental measurements always report the surface excess amount. Hence, based on the experimental measurements the surface excess weight percentage of hydrogen uptake in MOF-177 at 70 bar and 77 K was taken to be 7.5 wt.%. The calculated absolute adsorbed value was 11 wt.%, which may be technologically relevant.

The temperature dependence of hydrogen adsorption is a major consideration for storage applications [133]. The adsorption capacity decreases rapidly with increase in temperature and is barely detectable above 193 K. Also, it

is not clear from the results available to date that increasing the pressure will be sufficient to increase the adsorption capacity at ambient temperatures to a similar level as that achieved at 77 K. Better uptake capacity at moderate operating temperatures is a challenge that needs to be overcome before MOFs can be viable.

Improvement in hydrogen adsorption capacity requires a better understanding of optimization of adsorption sites. Kinetic trapping of hydrogen occurs in MOFs where the pore size is small enough to prevent desorption and at the same time the pore volume is large enough so that more hydrogen can be stored [134]. Hydrogen can be adsorbed at high pressures and then stored at lower pressures thus improving the temperature dependence of adsorption. Design strategies are necessary for synthesis of MOFs with improved adsorption capacity, enhanced H_2—surface site interactions with higher enthalpies of adsorption and improved kinetic trapping characteristics. Impregnation of MOFs, catenation (interpenetration of two or more frameworks that leads to reduction of the free diameter of pores), and the inclusion of open metal sites are possibilities that could enhance the storage properties [151]. Increasing the heat of adsorption would take MOFs to a quasi-chemisorptive regime in which a higher energy interaction between hydrogen and framework exists but remains short of true chemical bonding. In summary, a material with high gravimetric and volumetric hydrogen capacity should have high surface area with pores $\sim$0.28–0.35 nm in diameter and a large heat of adsorption (>15–20 kJ/mol) [151]. Catalyzed dissociative adsorption of hydrogen, such as that observed by Li and Yang [142, 143], increases the interaction energy as well as the volume fraction that can be penetrated by adsorbed hydrogen [134], which in turn would increase the storage capacity.

A few years ago, it was a challenge synthesizing MOFs in large quantities. Recently efforts have been made for large scale ($\sim$kg) production [130, 152, 153]. Since MOFs are crystalline, quality control can be obtained by X-ray diffraction, which can determine the degree of crystallinity and provide information about the shape and size of the pore.

Carbon and carbon-based nanostructures

Nanostructured carbon materials such as carbon nanofibers (CNFs) or graphite nanofibers (GNFs), CNTs (SWNTs and MWNTs), and carbon nanoscrolls (CNS) exhibit novel properties and have been a subject of various investigations for hydrogen storage.

Carbon nanofibers: CNFs or GNFs consist of stacks of graphite platelets arranged perfectly parallel to each other having an interlayer distance of 0.335 nm [154, 155]. The GNFs are of three types:

- Tubular—the graphite platelets are parallel to the fiber axis
- Platelet—the graphite platelets are perpendicular to the fiber axis
- Herringbone—the graphite platelets are at angle to the fiber axis

The length of GNFs can vary between 5 and 100 μm and their diameter between 5 and 200 nm [156]. GNFs have the capability of adsorbing hydrogen due to their large surface area as well as the inherent strong attractive intermolecular force between carbon and hydrogen [154, 157–160].

In 1998, Chambers et al. [155] reported an exceptionally high value of hydrogen adsorption in GNFs. They claimed that the material adsorbed 20 L hydrogen/g of carbon at 122 bar and 25 °C, which is equivalent to more than 60 wt.%. Since then, many experimental as well as computational studies have been conducted, but the exceptionally high values reported by Chambers et al. have not been corroborated. Ahn et al. [161] synthesized GNFs and measured desorption and adsorption properties at 77 and 300 K. The absolute level of hydrogen desorption measured was typically <0.01 H/C atom. Strobel et al. [162] were also unable to confirm the high storage capacity values of CNFs. Poirier et al. [163] studied hydrogen adsorption in various carbon nanostructures including nanofibers. They found that at room temperature CNFs could adsorb merely 0.7 wt.% at 105 bar. In 1999, Chen et al. [164] reported a large hydrogen uptake in CNTs and even graphite doped with alkali metals. However, Yang [165] subsequently attributed most of the weight uptake to moisture by conducting experiments both under wet and dry hydrogen flow.

Lueking et al. [166] conducted a detailed investigation of the hydrogen storage behavior of GNFs subjected to various pretreatments. They found that nanofibers possessing a herringbone structure and a high degree of defects were best for hydrogen storage. At room temperature and 69 bar, the maximum hydrogen desorption was measured to be 3.8 wt.%. In another study, the same group [167] suggested that selective exfoliation of a nanofiber could be used as a means to control the relative binding energy of the hydrogen interaction with carbon and thus vary the adsorption temperature. The GNFs were mixed with an acid solution (H_2SO_4 + HNO_3) for 2 h, filtered and then heated to 700 and 1,000 °C for various times. The 1,000 °C treatment resulted in a 10 times increase in the specific surface area.

Blackman et al. [168] studied the effect of surface area on adsorption capacity but did not find any direct correlation between the two. This is in contrast to the theory of physisorption, where the amount of gas adsorbed is linked to the specific surface area. The authors proposed that both

physical as well as chemical properties must be considered while designing and selecting carbon-based nanomaterials for hydrogen storage. With the purpose of enhancing hydrogen storage capacity, 2 wt.% Pd-doped nanofibers were prepared by Marella and Tomaselli [169]. After loading at 77 bar, a hydrogen storage of 1.38 wt.% was measured at room temperature. Other investigations of the hydrogen storage properties of GNFs reported that at room temperature and 80–100 bar the maximum hydrogen capacity was <0.2 wt.% [170, 171]. These values are low and a long way from published DOE targets and hence GNFs do not seem to be suitable for on-board hydrogen storage.

Gupta et al. [172] synthesized well aligned GNF bundles by using Pd sheets as catalysts as shown in Fig. 26. They found that these materials were easier to hydrogenate as compared to coiled fibers and showed a hydrogen storage capacity of 17 wt.% at 81 bar and room temperature. This high storage capacity was attributed to the expansion of graphitic sheets during hydrogenation allowing multilayer hydrogen adsorption. This would suggest an avenue to explore in order to achieve reasonable storage capacity in GNFs at moderate temperature and pressure.

Carbon nanotubes: CNTs are molecular-scale tubes of graphitic carbon. They may be single walled (SW) or multi walled (MW). A SWNT is a single atom thick layer of graphite rolled into a seamless cylinder. The diameter of a SWNT is a few nanometers and they have lengths that are several orders of magnitude larger. SWNTs can be one of three types:

- Arm-chair
- Zig-zag
- Chiral

MWNTs consist of multiple layers of graphite rolled in on themselves to form a tube. The interlayer distance in MWNTs is approximately 0.33 nm. Density functional theory calculations show that at room temperature hydrogen adsorption in SWNT cannot exceed 7.7 wt.% even when contributions from chemisorption of hydrogen on carbon are considered [173]. Assuming only physisorption of hydrogen in CNTs, it would be impossible to achieve this amount of adsorption at room temperature.

In 1997, Dillon et al. [174] first investigated the hydrogen storage of non-purified bundles of SWNTs and reported a gravimetric density of 5–10 wt.%. Ye et al. [175] reported a storage capacity of 8 wt.% for purified SWNTs at 80 K and a hydrogen pressure of 130 bar. SWNTs were purified by sonicating for 10 h in dimethyl formide followed by vacuum degassing for 10 h at 220 °C. Liu et al. [176] showed by volumetric measurements on SWNT with mean diameter of 1.85 nm a storage capacity of 4.2 wt.%. They also reported that about 78.3% of the stored hydrogen could be released under ambient pressure at room temperature. However, such high values for storage capacity have not been reproduced. A lower hydrogen storage capacity of 2.3 wt.% at 77 K was reported by Panella et al. [160] for SWNTs.

Xu et al. [171] experimentally measured hydrogen storage capacity of various carbon materials, including AC, single walled carbon nanohorn (a tubule with a cone cap, resembling a horn), SWNTs, and GNFs at 303 and 77 K. At room temperature the hydrogen capacity was <1%. At 77 K, the AC had maximum capacity of 5.7 wt.% at a pressure of 30 bar. Carbon materials adsorb hydrogen gas through non-dissociative adsorption on the surface and hydrogen storage capacity is proportional to their specific surface area and the volume of micropores as shown in Fig. 27 [160, 171, 177, 178]. The linear dependence of the storage capacity on specific surface area of carbon materials is independent of the nanostructure [160].

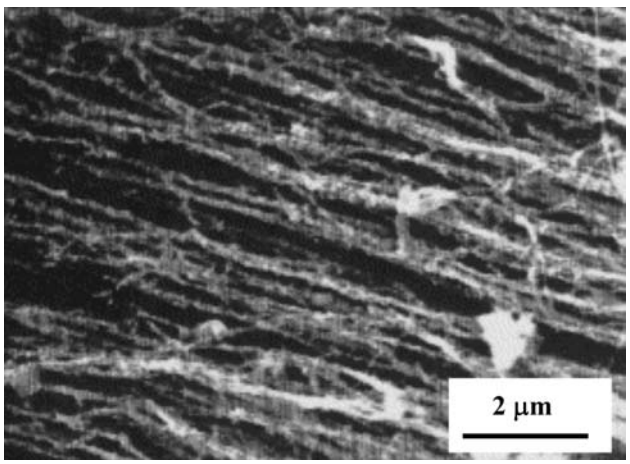

Fig. 26 SEM image showing aligned GNF bundles (reprinted from [172], copyright (2004) with permission from Elsevier)

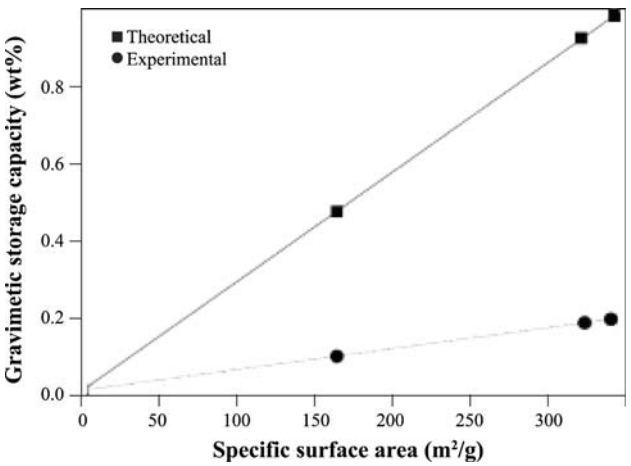

Fig. 27 Variation of the gravimetric storage capacity of CNTs with specific surface area (data from: [178]

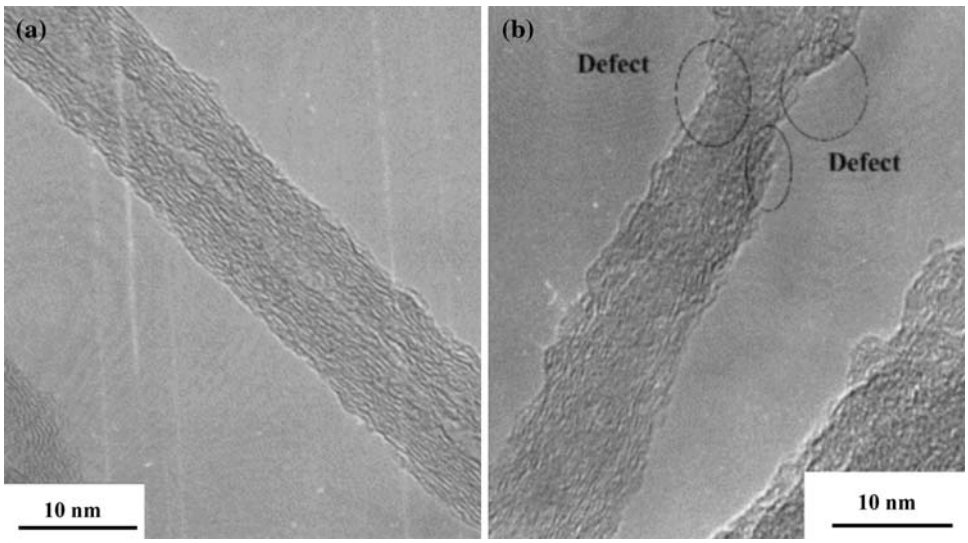

Fig. 28 TEM images of CNTs: (**a**) as prepared samples, (**b**) after annealing and K-treatment (reprinted from [180], copyright (2007) with permission from Elsevier)

The hydrogen storage capacity of CNTs could be improved when they are modified by an alkali metal such as K, Li, or Na. Chemical activation with KOH leads to an increase in the material porosity and the activated sample exhibits a texture similar to AC [179]. Chen and Huang [180] reported that MWNTs were found to be attacked by KOH forming pores of size 2–15 nm as shown in Fig. 28. The KOH-modified MWNTs showed a hydrogen storage capacity of 4.5 wt.% at ambient pressure and moderate temperature. The material was heated from 303 to 823 K and held for 1 h in a continuous flow of hydrogen then cooled to room temperature.

The MWNTs were prepared by catalytic decomposition of acetylene over a $Co_{0.05}Mg_{0.95}O$ catalyst followed by impregnation with KOH. Analysis of the nanotubes showed the presence of residual Co from the catalyst. The value of storage capacity was attributed to the alkali metal as well as the residual Co and the defect structures. The residual Co catalytically dissociated molecular hydrogen and facilitated adsorption on the outer surface. Residual Co was also suggested to facilitate adsorption in the inner layers through defect sites of CNTs [180]. However, no significant hydrogen uptake was observed by Wu et al. [181] in MWNTs that were synthesized by catalytic decomposition of CO and CH_4 on a Co/La_2O_3 catalyst. Strong dependence of the hydrogen storage capacity on the residual catalyst particles has also been reported for SWNT [182]. In SWNTs bundles treated with NaOH the preferred storage site for hydrogen molecule was the inter-tube space [183].

The hydrogen uptake capacity of 2.9 wt.% at 300 K and 4.1 wt.% at 77 K has been reported by Johansson et al. [184] for inter-grown nanotube like aggregates, multi walled nanobarrels at 100 bar. Zuttel et al. [185] reported a higher hydrogen storage capacity of 5.5 wt.% in MWNT at 77 K. However, this value dropped to 0.6 wt.% at room temperature. In a comparative study of hydrogen adsorption on MWNT and AC, Zhou et al. [186] found that the amount of hydrogen adsorbed on MWNT was 3–5 times smaller than that on AC. Also, the amounts of hydrogen adsorbed on both materials were very small. MWNT could adsorb only 0.14 wt % hydrogen at 298 K and 60 bar pressure. It should be noted that room temperature hydrogen adsorption capacity of CNTs is small and hence they do not appear to fit the requirements for on-board storage. In 2000, Pinkerton et al. [187] from General Motors measured hydrogen absorption in K- and Li-doped graphite, and Li-doped MWNT. The maximum hydrogen uptake of 1.3 wt.% was observed in K-doped graphite. The other materials did not show any significant hydrogen uptake. Moreover, weight gain was also observed in an argon atmosphere containing no hydrogen, and most of the weight gain observed in thermogravimetric analysis was due to moisture. Hence, they concluded that these materials are not capable of storing hydrogen in any "technologically useful form."

Like MOFs, hydrogen adsorption in CNTs can be enhanced by spillover. Figure 29 illustrates the mechanism of spillover where the Pt particle adsorbs and dissociates molecular hydrogen and the atoms diffuse through the active carbon support and subsequently adsorb on the CNT surface [188, 189]. The interaction energy of atomic hydrogen and SWNTs is higher than that for molecular hydrogen and it was found to be affected by tube diameter, chirality, and tube surface (i.e., interior or exterior surface). Molecular orbital calculations suggest that the binding energy is higher for larger tube diameters, exterior tube surface, and for zig-zag SWNT. Zacharia et al. [190] observed a 30% higher value of hydrogen capacity in CNTs doped with Pd and V as compared to pristine CNTs at 20 bar pressure and room temperature. The metal

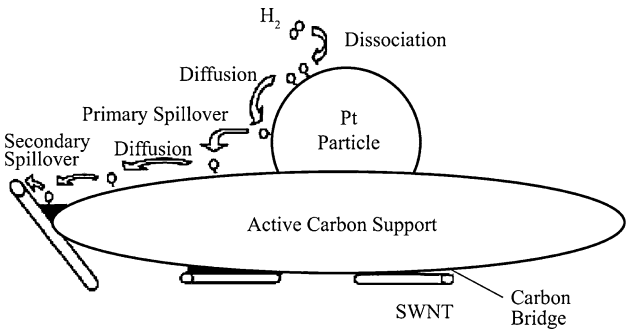

Fig. 29 Schematic illustration of the spillover mechanism (after: [188])

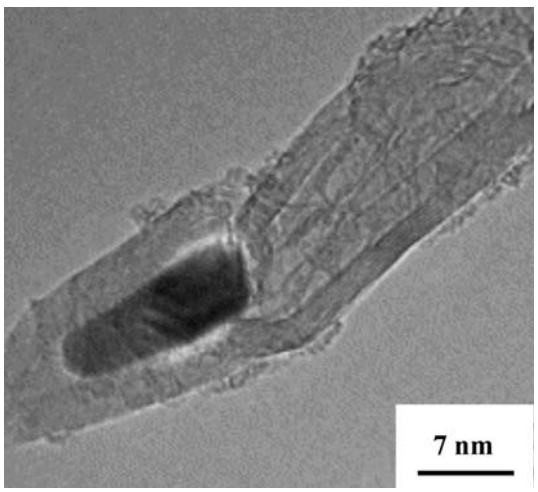

Fig. 30 TEM image of a palladium nanoparticle trapped inside doped CNT (reprinted from [190], copyright (2005) with permission from Elsevier)

particles enhanced storage capacity by spillover. The room temperature capacities of doped CNTs were however small (<0.7 wt.%). The smaller capacities were attributed to the metal particles being inside the nanotubes rather than on the exterior tube surface as shown in Fig. 30. In a recent investigation by the same authors, MWNTs embedded with nano-crystalline Pd have shown a maximum reversible hydrogen storage of 0.18 wt.% at 298 K and 16 bar [191]. Because the Pd nanoparticles were embedded inside the nanotubes there was no contribution of spillover. Anson et al. [192] reported that the maximum hydrogen capacity of Pd doped SWNT at 298 K and 1.01 bar was 0.4 wt.%. The hydrogen capacity increased with increasing Pd content.

Kowalczyk et al. [193] investigated the suitability of different pore size nanotubes for storage and separation of hydrogen-methane mixtures. The pore size depends on chirality. The nanotube bundles with wider nanotube diameter (>0.62 nm) were more effective and SWNTs with diameter of 0.68 nm were best suited for selective adsorption of hydrogen. Cao and Wang [194] predicted the gravimetric storage capacities for a diamond shaped bundle of SWNTs with a van der Waals gap of 0.6 nm. At 300 K and 121 bar, the storage capacity should be 2.5 wt.%. At 105 K and 132 bar, the same bundle of SWNTs might store up to 7.4 wt.% and 0.622 kg/L [194].

Figure 31 shows an SWNT-based nanocontainer designed by Ye et al. [195]. They demonstrated that hydrogen can be filled into the container upon compression at low temperature and locked inside after release of the external pressure. The internal pressure that was achieved in their design was 25 kbar and the H/C weight percent was 7.7%. The internal pressure produces isotropic (i.e., cylindrical) expansion. In such a process, the C–C bond distance is stretched, which requires very high energy. Hence, the nanotube can endure much higher internal pressure.

Hence, in order to be able to design CNTs for hydrogen storage one must be able to control the parameters such as pore size, chirality, tube length, specific surface area, open or closed ends, gap between individual nanotubes in a bundle, purity of the material, and nature of defects. Pre-treatment of the nanotube (by an acid or alkali) to create defect structures on the surface, and doping with metal nanoparticles can significantly affect hydrogen storage capacity.

The hydrogen storage capacity of some carbon nano-structures are summarized in Table 9. It is immediately

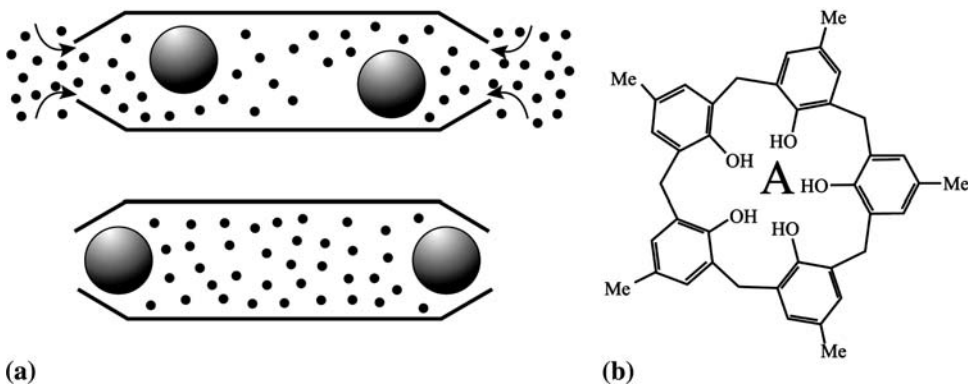

Fig. 31 (**a**) The design for a nanocontainer, with the cap and the ball (C60) together serving as a molecular valve that traps the hydrogen after the release of the external pressure. (**b**) The bowl-shaped calix[5]arene is used as the cap for the container, with its center, labeled as A, being one of the leaks (reprinted from [195], copyright (2007) with permission from Elsevier)

Table 9 Hydrogen storage capacity of various carbon nanostructures

References	Material	Temp (K)	Pressure (bar)	Maximum storage (wt.%)
Anson et al. [192]	SWNT (Pd loaded)	298	1.01	0.4
Blackman et al. [168]	CNF (activated by KOH)	303	100	0.35
Cao and Wang [194]	SWNT (diamond shaped bundle)	300	121	2.5
		105	132	7.4
Chambers et al. [155]	GNF	298	113	65
	GNF (tubular)	298	113	11.26
	GNF (herringbone)	298	113	67.55
	GNF (platelet)	298	113	53.68
Chen et al. [178]	MWNT	Moderate temp	1.01	0.71
	MWNT (modified by KOH)			4.47
Costa et al. [182]	SWNT (Ni)	77	60	0.103
		298	60	0.018
	SWNT (Ni(16.21), Y(3.26))	77	60	0.195
		298	60	0.037
	SWNT (Ni(25.35), Y(1.65))	77	60	0.599
		298	60	0.115
Gupta et al. [172]	GNF (Pd catalyst)	300	81.1	17
Hong et al. [170]	GNF	RT	80	0.11–0.18
Johanson et al. [184]	MWNB	77	100	4.1
		300		2.9
	ANPC	77		3.3
		300		2.6
Liu et al. [176]	SWNT	298	100	4.2
Lueking et al. [167]	GNF (exfoliated by acid mixture followed by thermal shock)	300	20	0.29
Lueking et al. [166]	GNF (herringbone)	Desorption studies		
Marella and Tomaselli [169]	GNF (doped with 2 wt.% Pd)	RT	77	1.38
Panella et al. [160]	SWCNT (purified)	298	70	0.4
		77	30	2.3
	AC	298	70	0.7
		77	30	4.5
Poirier et al. [163]	CNF	295	105	0.7
Rather et al. [191]	MWNT (Pd embedded)	298	16	0.18
Shiraishi et al. [183]	SWNT	Desorption study		
Strobel et al. [162]	AC	296	125	1.6
	CNF	296	125	1.2
Xu et al. [171]	AC	303	100	0.7
	ACF	303	100	0.5
	SWNH (pure)	303	100	0.22
	SWNH (treated with HNO_3)	303	100	0.35
	SWNH (oxidized at 773 K)	303	100	0.55
	SWNT (as prepared)	303	100	0.3
	SWNT (purified)	303	100	0.5
	SWNT (treated with HNO_3)	303	100	0.35
	GNF ($Ni_{0.5}Cu_{0.5}$ catalyst)	303	100	0.22
Yang et al. [188]	SWNT	298	110	0.48
	SWNT/Pt-AC/carbon bridge	298	110	0.4
Ye et al. [175]	SWNT (crystalline ropes)	80	70	8.25

Table 9 continued

References	Material	Temp (K)	Pressure (bar)	Maximum storage (wt.%)
Ye et al. [195]	SWNT based nanocontainer (theoretical)		25 kbar (internal)	7.7
Zacharia et al. [178]	MWNT	298	16	0.07
	SWNT	298	16	0.15
Zacharia et al. [190]	CNT (V-doped)	RT	20	0.69
	CNT (Pd-doped)	RT	20	0.66
Zhou et al. [186]	MWNT	233–318	100	0.23–0.27
		233–318	60	0.175–0.14
	AC	233–298	60	0.5–0.89
Zuttel et al. [177]	SWNT (calculated)			3
Zuttel et al. [185]	CNT	77		5.5
		RT		0.6

obvious that there is a huge disparity in the results. Hydrogen storage capacity is measured by volumetric or gravimetric methods both of which are prone to errors and a possible source of discrepancy in the results. Most of the inconsistencies in the data have been attributed to impurities and the limited quantities of the various nanotube samples as well as experimental errors in the measurements [154, 196, 197]. Also, an accurate method for measurement of hydrogen adsorption and storage capacity is required. Two different volumetric apparatus for the measurement of hydrogen capacity have been constructed by Zhang et al. [196] and Kiyobayashi et al. [198]. Both the groups claim that their methods give accurate value of the uptake of hydrogen. However, no significant hydrogen storage capacity was measured in either case.

Carbon nanoscrolls: CNS is a class of nanostructured carbon that can be schematically obtained by twisting a graphite sheet. They are very similar to MWNT, showing a similar intralayer distance of ~0.36 nm. The key difference between MWNT and CNS is that in the latter the intralayer distance can vary. CNS was first reported as a new material for hydrogen storage in 2003 [199]. Braga et al. [200, 201] showed by molecular dynamic simulations that hydrogen can be adsorbed at 77 K but no significant adsorption takes place at 300 K. The stored hydrogen can be desorbed by increasing the temperature to about 400 K. These nanoscrolls had internal diameter of 2 nm and interlayer distance of 0.34 nm. In one of their very recent computational studies on CNS, Mpourmpakis et al. [202] reported that pure CNS could not accumulate hydrogen because the interlayer distance was very small. However, alkali doping introduced an opening of about 0.7 nm in the spiral structure. The doped CNS had the hydrogen storage capacity of 3 wt.% at ambient temperature and pressure. The study of CNS for hydrogen storage is a new area and further investigations are required to assess the suitability of this material for hydrogen storage.

Synthesis of carbon nanostructures: carbon nanostructures, especially CNTs, can be synthesized via three different routes:

- Arc discharge
- Laser ablation
- Chemical vapor deposition (CVD)

The arc discharge method was first reported by Iijima in 1991 [203]. However, the major drawback of this method is its low yield, ~25%. Laser ablation of graphite in inert atmosphere at 1,200 °C in the presence of transition metal catalyst was developed by Smalley and colleagues [204, 205] for fabrication of CNTs. The yield of SWNT was about 50%. However, this method is more expensive than arc discharge and CVD. In CVD, catalytic decomposition of a carbon-containing gas (acetylene, ethylene, ethanol, methane, etc.) at temperatures between 600 and 1,000 °C leads to the formation of CNTs, which grow on metal catalyst sites [206]. These methods are capable of producing large quantities of CNTs. However, they are not economical and involve large energy inputs. Both laser ablation and CVD require high temperatures.

Other hydrogen storage materials

As discussed in the preceding sections, various MOFs and carbon-based nanostructures have been identified for hydrogen storage by physisorption. However, one major drawback of these materials is the low adsorption temperature and the high pressures required. Additionally, the hydrogen capacity values for carbon nanostructures are not reproducible and as seen from Table 9, there is a huge disparity in the reported values.

Oxide nanostructures may be alternatives to MOFs and carbon nanostructures for room temperature storage by physisorption. Various oxides such as B_2O_3, SiO_2, and NiO have indeed been recognized as materials capable of hydrogen uptake [207–209]. Theoretical calculations yielded a value of 12 kJ/mol for the heat of adsorption of hydrogen on B_2O_3 [207]. This value suggests strong interaction between the material and the physisorbed hydrogen, which in turn increases the adsorption temperature. Theoretical studies also suggest that these oxides have surface properties that make them particularly suitable for hydrogen uptake [210, 211].

Wang et al. [212] have synthesized SiO_2 nanosprings and studied their hydrogen storage properties. These nanosprings were grown by the vapor–liquid–solid mechanism facilitated by Au nanoparticles. The synthesis temperature can be as low as 325 °C and atmospheric pressure, which is much lower than that required for the synthesis of carbon nanostructures. Examples of the nanospring morphology are shown in Fig. 32. Hydrogen was found to adsorb onto the nanosprings at 25 °C and be released at 100 °C. Using X-ray photoelectron spectroscopy the hydrogen was shown to attach preferentially at Si sites on the nanospring surface. What is perhaps most significant about this material is that multilayer adsorption of hydrogen is possible (which does not occur on CNTs). Assuming formation of only two monolayers, a gravimetric capacity >5% would be possible. Multilayer adsorption is critical to the use of nanostructured materials for non-dissociative hydrogen storage.

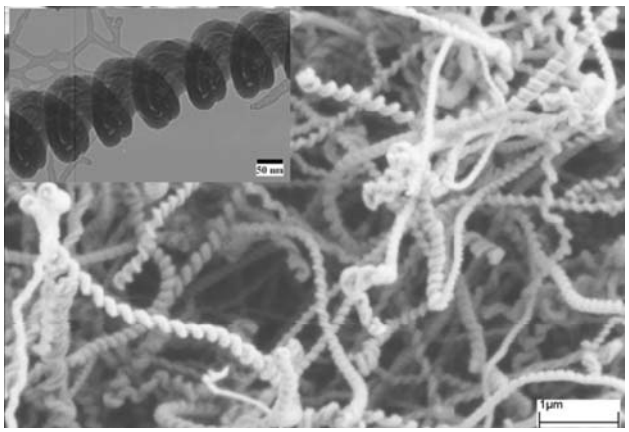

Fig. 32 SEM image of as-grown silica nanosprings. The inset is a bright-field TEM image of an individual silica nanospring, which shows that it is formed from multiple, intertwined, nanowires (courtesy: D.N. McIlroy]

Fuel cell

Fuel cells directly transform the chemical energy carried by hydrogen into electrical energy. They are electrochemical cells fed with hydrogen, which is oxidized at the anode. Oxygen from air is reduced to water at the cathode. The development of fuel cells is considered to be an integral part and final step of a sustainable hydrogen economy. Although they were invented one and a half centuries ago, only recently has it become feasible for them to compete with existing energy production systems [213]. They are capable of achieving efficiencies as high as 80%, they are non-polluting, and provide electrical power that can be tailored to a wide variety of applications—from large stationary power plants, to transportation vehicles, to consumer devices like cell phones and personal computers. The basic fuel cell types cover a varying range of operating conditions and performance specifications as shown in Table 10.

Among the various types of fuel cells, proton exchange membrane fuel cells (PEMFCs) have potential to become a viable power source for transportation because of their low operating temperatures (60–80 °C) and relatively high power density. The protons released during oxidation are conducted through a polymer membrane to the cathode,

Table 10 Types of fuel Cell types and their operating features

Fuel cell type	Electrolyte	Conducting ion	Temp (°C)	Efficiency (%)	Output (kW)	Features
Polymer (PEM)	$CF(CF_2)_nOCF_2SO_3^{2-}$	H^+	60–80	40–50	50–250	High power density, Pt catalyst, must be kept wet, poisoned by CO
Alkaline	KOH	OH^-	90	70	0.3–5	High power density, cannot tolerate CO_2
Phosphoric acid	H_3PO_4	H^+	200	40–80	200	Medium power density, Pt catalyst, sensitive to CO
Molten carbonate	Li_2CO_3/K_2CO_3	CO_3^{2-}	650	60–80	2 MW	Low power density, Ni catalyst, needs CO_2 recycle
Solid oxide	$Zr_{0.92}Y_{0.08}O_{1.96}$	O^{2-}	700–1000	60	100	Medium to high power density, accepts CO as fuel
Direct methanol	$CF(CF_2)_nOCF_2SO_3^{2-}$	$H^+(H_2O, CH_3OH)$	60–120	–	–	Medium power density, low efficiency, high Pt content

Table 11 DOE freedomCAR targets for FC stack material (data from: [214])

Fuel cell stack targets		Year	
Parameter	Units	2010	2015
Power density	mW/cm^2	1,280	1,280
Durability	Hours	>5,000	>5,000
Precious metal loadings	g/kW	0.3	0.2
Precious metal cost	$/kW	<3	<3
MEA cost	$/kW	10	5
Degradation	%	10	10
Time to rated power			
−20 °C Ambient temperature	Seconds	30	30
20 °C Ambient temperature	Seconds	15	15
Survivability	°C	−40	−40

whereas the electrons travel along an external electrical circuit, thus generating current. A typical PEMFC membrane electrode assembly (MEA) comprises two electrodes (anode and cathode) and electrode catalyst layers separated by a proton conducting membrane. The electrodes are supported by backing layers of a porous carbon gas diffusion layer (GDL), which ensures effective diffusion of the gases to the catalyst. While low temperature operation allows quick startup and results in high durability, it also adds to the need for highly sensitive metal catalysts (typically Pt) to split hydrogen. Pt is expensive and costs are currently >$75/g.

Although fuel cells offer many advantages for a diverse set of applications, so far they have been introduced only on a limited scale and at high cost. Most of the obstacles in the widespread implementation of fuel cell technology are related to the need for inexpensive, more durable materials that have better operating characteristics, especially in the case of the electrode catalysts and membranes (ionic conductors). The DOE has set targets for fuel cell stack materials for automotive application (Table 11). The target for power density for the year 2010 and 2015 is 1.28 W/cm^2, and that for the cost of MEA are $10 and $5/kW, respectively. In 2007, the lowest MEA cost achieved was $22/kW, which is more than double the target costs for 2010. The highest power density of PEMFC achieved so far is about three times smaller than the DOE target for 2010 and 2015 [214]. Improving the power density as well as reducing the cost is essential before hydrogen fuel cells can be commercially used in automobiles.

Electrode catalyst

The catalyst layers in PEMFCs typically contain nanoscale Pt or Pt-alloy particles on a high surface area support such as carbon black [215]. Reducing the use of Pt is a major requirement for wide-scale commercialization of these devices, especially for use in automobiles. Reducing the size of catalyst particles results in larger surface area, which in turn creates a large number of catalytically active sites [215]. However, during conventional sol–gel processing methods, Pt particles tend to agglomerate and form clusters. Further reduction in particle size and high dispersion is essential to reduce the amount of metal used. Chen and Xing [213] developed a method that uses poly-(vinylpyrrolidone) (PVP), to prevent particle aggregation and achieved a high dispersion. It was found that Pt nanoparticles mediated by PVP were smaller than those obtained without PVP and they had a narrower size distribution (see Table 12). Metal loadings up to 35 wt.% were obtained on carbon black.

Table 12 Effect of PVP on Pt nanoparticle size of the 20 wt.% Pt/C catalyst (data from: [213])

PVP:Pt	Particle size (nm)
0	3.87
0.1	2.30
1.0	2.48

Sputter deposition has been examined as a means of reducing cost by achieving ultra low levels of catalyst loading. Alvisi et al. [216] deposited nano-sized (diameter 2–5 nm) Pt clusters on gas diffusion electrodes (carbon paper plus a polytetrafluoroethylene (PTFE)/C diffusive layer) by sputtering. Radev et al. [217] used dc magnetron sputtering as a technique for making thin film Pt electrodes with homogeneous particle distribution and controlled metal loading.

Very recently, Zeis et al. [218] fabricated Pt-plated nanoporous gold leaf (Pt-NPGL) by coating a conformal, atomically thin skin of Pt over the high surface area pores of a thin membrane of nanoporous gold. Since Pt loading in Pt-NPGL could be controlled down to 10 μg/cm^2, it was suggested that the material holds promise as a low Pt loading, carbon-free electrocatalyst. Such a material can be used both as electrode and catalyst. This approach may also prevent particle aggregation and thus result in high dispersion and smaller nanoparticles.

The oxidation reduction reaction (ORR) of water at the cathode is an important step in the generation of an electric current in PEMFC. The rate of reaction is slow even when Pt is used as a catalyst. Hence, developing alternatives to Pt for ORR can be another avenue for reducing cost. Alternative catalysts based on pyrolyzed iron, carbon, and nitrogen compounds, such as Fe—phenanthroline ($C_{12}H_8N_2$) complexes, show an activity comparable to commercial Pt catalysts [219, 220]. Matter and Ozkan [221] prepared

non-metal catalysts for ORR by decomposition of acetonitrile vapor at 900 °C over a pure alumina support and supports containing 2 wt.% Fe or 2 wt.% Ni on alumina. The sample prepared with Fe was the most active. However, nitrogen-containing carbon deposited on pure alumina (which contained <1 ppm metal contamination) also showed comparable activity. Hence, it was concluded that Pt or Fe is not required for ORR activity. Subsequently, Matter et al. [222] investigated the role of non-noble metal particles such as Fe and Ni on the formation of various nitrogen-containing carbon nanostructures and their ORR activity and found that Fe-doped precursors were the best precursors for active catalysts. Matter et al. [223] recently prepared nitrogen-containing carbon nanostructures from the decomposition of acetonitrile at 900 °C over silica and magnesia support impregnated with Fe, Co, or Ni. Carbon grown from supported Fe and Co particles consisted of compartmentalized fibers with a stacked cup structure, while mostly broken MWNTs formed from Ni particles (Fig. 33). Activity for ORR was highest for fibers grown from supported Fe and Co particles, which may be related to edge plane exposure.

Various attempts have been made to synthesize catalysts for ORR consisting of Pt nanoparticles supported on CNTs. The CNTs are expected to facilitate charge transfer and therefore enhance the performance of fuel cells. Liu et al. [224] prepared two Pt/C catalysts consisting of Pt nanoparticles (2–6 nm) supported on carbon black and CNT with 20 wt.% metal loading (Fig. 34). These were prepared by microwave assisted rapid heating. Preliminary tests with a single stack fuel cell indicated that both Pt/C catalysts had better electrocatalytic activity. Girishkumar et al. [225] fabricated an MEA for hydrogen fuel cells using SWCNTs support and Pt catalyst. Films of SWCNTs and commercial Pt black were sequentially cast on a carbon fiber electrode (CFE) using electrophoretic deposition. The maximum power density obtained using CFE/SWCNT/Pt electrodes as both the anode and the cathode was ~20% better than that using the CFE/CB/Pt electrodes. On the other hand, a previous effort of Glora et al. [226] to make electrodes with carbon aerogels was not successful as the power density observed with such electrodes was a factor of 6 lower than conventional electrodes. This is in contrast to the

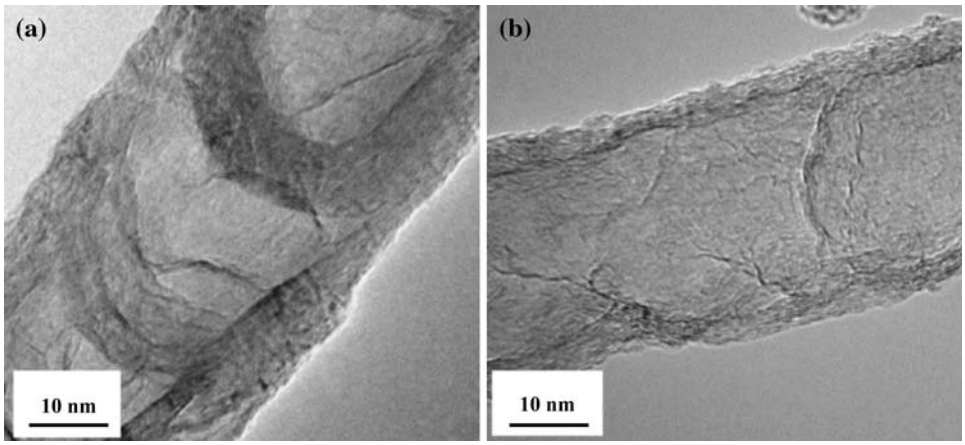

Fig. 33 TEM images showing CN_x structures formed from (**a**) Fe or Co particles, (**b**) Ni particles (reprinted from [223], copyright (2007) with permission from Elsevier)

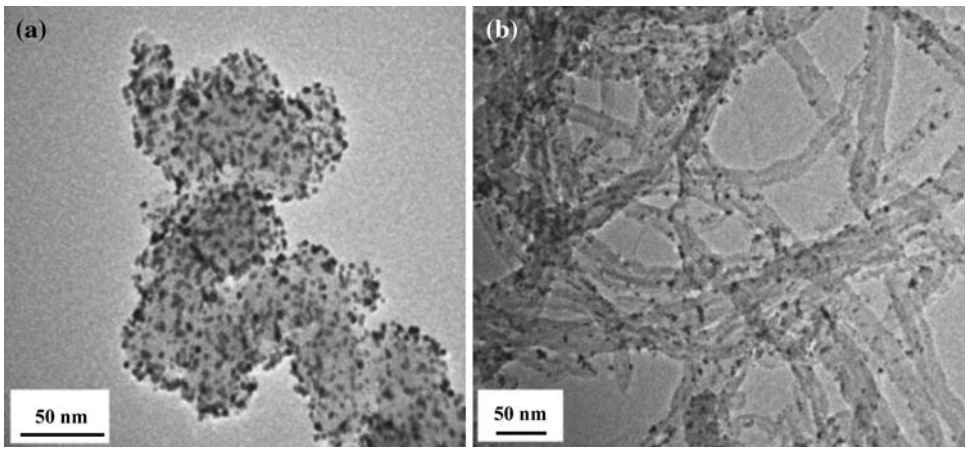

Fig. 34 TEM images of microwave-synthesized Pt nanoparticles supported on (**a**) Vulcan XC-72 carbon, (**b**) CNTs (nominal Pt loading 20 wt.%) (reprinted from [224], copyright (2005) with permission from Elsevier)

observations of Liu et al. [224]. The difference is due to the Pt particle size of 20–30 nm, which is 5–10 times larger than the particle size obtained by Liu et al. [224].

Very recently, Caillard et al. [227] synthesized four fuel cell cathodes on carbon paper and PTFE/carbon-loaded cloth GDL, both with and without CNFs. Pt/CNFs nanostructures grown on PTFE/carbon-loaded cloth showed best performances. Although the power density of sputtered Pt/CNF cathode was a little lower than the conventional one (300 vs. 370 mW/cm^2), its Pt utilization efficiency was four times higher. Yuan and Ryu [228] prepared CNTs and CNFs with different size and morphology to be used as support for Pt catalysts. Fuel cell performance with twisted CNFs was better than that with straight CNFs, and the performance of CNTs and CNFs increased for smaller diameters. The best performance, a voltage of 645 mV at a current density of 500 mA/cm^2, was given by twisted CNFs with diameter 65 nm.

Low CO tolerance is another limitation of fuel cells consisting of Pt/C catalyst. A thin layer of Ru deposited on the surface of the electrode can act as a filter for CO thus improving tolerance of the fuel cell. Also, nanocrystalline PtMo/C catalysts have been reported to show a two to three times improvement in CO tolerance in a PEMFC as compared to the conventional Pt–Ru/C electrocatalysts [229].

Membrane

The prime requirements of PEMFC membranes are high proton conductivity, adequate mechanical strength and stability, good chemical, and electrochemical stability under operating conditions, moisture control in stack, low H_2 and O_2 crossover, and moderate production cost [230]. Nafion is the most widely used membrane. Its performance depends on the level of hydration—the higher the hydration, the higher the conductivity. However, with higher levels of hydration there is a possibility of flooding the electrode, which can adversely affect cell performance. Reduction in membrane thickness is one way of overcoming this problem. This also reduces membrane resistance to proton conduction. However, there is a limit to which the thickness can be reduced because of the risk of H_2 and O_2 crossover through very thin membranes. It was suggested by Watanabe et al. [231] that the difficulties with management of water content and reactant crossover can be overcome by incorporating the PEM membranes with nanometer size particles of Pt and/or metal oxides. The Pt particles prevent reactant crossover by recombination of H_2 and O_2 to form water. On the other hand, the oxide particles could absorb any water that was produced at Pt particle or back diffused from the anode. A method for incorporating TiO_2 into Nafion [232], which consists of four steps:

- Pretreatment of normal-PEM converting to Na^+ form
- Impregnation of Ti-alkoxide into the PEM
- Controlled hydrolysis of Ti-alkoxide to form TiO_2 particles
- Treatment of TiO_2-PEM to obtain the H^+ form

Chen et al. [233] prepared Nafion/TiO_2 composites with mesoporous TiO_2. As seen from Table 13, the composite made with TiO_2 with the highest surface area showed the largest power density and the best cell performance. Attempt has also been made to include a layer of TiO_2 as a spacer between Nafion and the Pt catalyst [234]. The presence of TiO_2 layer as thick as 18 nm did not seem to affect the cell performance. It was therefore suggested that it may be possible to replace Nafion in PEMFC by TiO_2.

Better water absorption and retention capabilities of membranes at temperatures >90 °C is of particular interest for higher temperature operation of fuel cells. It has been reported that the addition of nanoparticles of oxides such as ZrO_2, TiO_2, and SiO_2 results in improvement of water retention properties of Nafion at 90 °C [235–237] (Fig. 35).

Table 13 Variation of power density with specific surface area of TiO_2 (data from: [233])

TiO_2 samples	SSA of TiO_2 (m^2/g)	Power density of Nafion + 3 wt.% TiO_2 samples (mW/cm^2)
T_{PF6}	122	893
T_{BF4}	82	644
$T_{conventional}$	89	714
T_{P25}	46	543

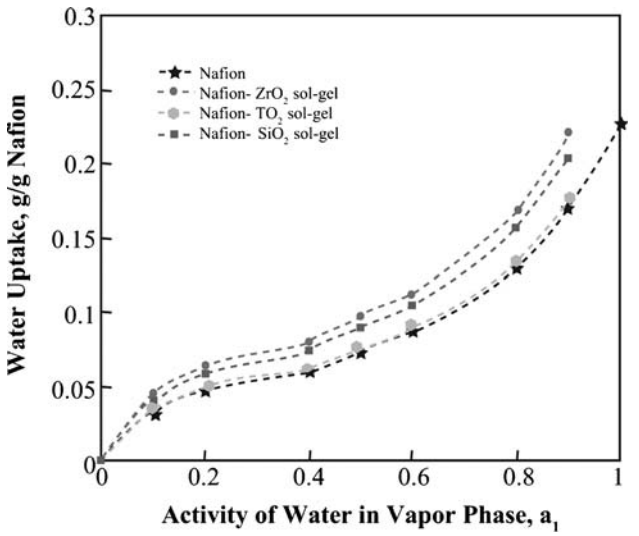

Fig. 35 Effect of various oxide particles on water retention properties of membrane (data from: [235–237])

As described in the preceding sections, the major issues regarding the commercialization of fuel cells are the reduction in cost by reducing precious metal loading while maintaining the catalytic activity for ORR reaction; and improving the conductivity and water retention properties of the PEM. Further reducing the size of Pt nanoparticles by innovative synthesis methods can reduce the overall cost. Development of alternative catalysts with activities similar to Pt can also help reduce costs. The ORR activity can be enhanced by supporting catalysts on carbon nanostructures, especially CNFs. The water retention properties of the PEM can be enhanced by incorporating nanoscale particles of oxides that have hygroscopic properties.

Summary and conclusions

In summary, nanostructures and nanoscale processes appear ideally suited for enhancing the performance of catalysts and electrodes for solar hydrogen production, hydrogen storage materials, and membrane electrode assemblies for fuel cells. Solar hydrogen production is being considered an option for long term hydrogen production due to the abundance of both water and sunlight. The role of nanotechnology in enhancing the process efficiency is becoming increasingly significant. Nanostructures of cheaper and abundant semiconducting metal oxides such as TiO_2, ZnO, and Fe_2O_3 may make photocatalytic and photoelectrochemical hydrogen production economically viable. The major challenge is to develop and design low-cost methods that produce easy-to-handle nanomaterials with high surface area and high porosity. TiO_2-based nanostructures, particularly ordered arrays of high aspect ratio nanotubes appear to enhance solar to hydrogen conversion efficiency. Modifying these nanostructures with carbon can further improve efficiency. Dye-sensitized photoelectrochemical cells based on nanocrystalline TiO_2 are being developed for solar hydrogen production. Research is needed to develop suitable passivation techniques to prevent photocorrosion of conventional solar cell materials, which at present possess higher efficiencies but are unstable in aqueous solutions.

The main process in solid state hydrogen storage is the interaction between the hydrogen and the surface of the storage medium. Because of their enormous surface area nanostructured materials can enhance the efficiency of this process and hence improve the storage capabilities. Nanostructured Mg and Mg-based hydrides store hydrogen by chemisorption. Various efforts have been made to enhance their hydrogen storage properties, including mechanical milling, alloying, addition of graphite, metal oxides, and CNT. However, it is not certain whether this enhancement is a size effect, a catalytic effect, or a combined effect. A more meticulous investigation is required for delineating the influence of these factors and to optimize the effects of grain size and additives. Thermodynamic analyses of Mg-based systems are also essential for understanding and precisely predicting the effect of these modifications.

MOFs and carbon nanostructures store hydrogen by a non-dissociative process, physisorption. The major drawback of these nanostructures is that they can only store any detectable amount of hydrogen at lower temperatures (<100 K). Additionally, the hydrogen storage capacity values of carbon nanostructures are not reproducible. Improving the temperature dependence requires a better understanding of the adsorption sites. Design strategies and modifications are required to enhance hydrogen–surface interaction and increase enthalpies of adsorption. Doping with metal particles may be effective in enhancing storage capabilities by spillover. Multilayer hydrogen adsorption is another avenue to explore for enhancing the storage capabilities of these nanostructures. Multilayer adsorption has been demonstrated in one dimensional oxide nanostructures.

PEMFCs have the potential to become a viable power source for transportation. The major issues regarding the commercialization of fuel cells are the reduction in cost by reducing Pt loading in the electrode and improving the conductivity and water retention properties of the membrane. Reducing the size of Pt nanoparticles by innovative synthesis methods and development of alternative catalysts can reduce the overall cost. The water retention properties of the membrane can be enhanced by incorporating nanoscale particles of hygroscopic oxides.

References

1. http://www.eere.energy.gov/afdc/fuels/hydrogen_alternative.html
2. Ewan BCR, Allen RWK (2005) Int J Hydrogen Energy 30:809. doi:10.1016/j.ijhydene.2005.02.003
3. Sherif SA, Barbir F, Veziroglu TN (2005) Sol Energy 78:647. doi:10.1016/j.solener.2005.01.002
4. Satyapal S, Petrovic J, Read C, Thomas G, Ordaz G (2007) Catal Today 120:246. doi:10.1016/j.cattod.2006.09.022
5. Basic Research Needs for Hydrogen Economy Report of the Basic Energy Sciences Workshop on Hydrogen Production, Storage and Use, 3–15 May 2003. http://www.sc.doe.gov/bes/reports/files/NHE_rpt.pdf
6. Schlapbach L, Zuttel A (2001) Nature 414:353. doi:10.1038/35104634
7. http://www1/eere.energy.gov/hydrogenandfuelcells/pdfs/doe_h2_production.pdf
8. Nowotny J, Bak T, Nowotny MK, Sheppard LR (2007) Int J Hydrogen Energy 32:2609. doi:10.1016 j.ijhydene.2006.09.004
9. Boer KW (1977) Sol Energy 19:525. doi:10.1016/0038-092X(77)90109-8
10. Bird RE, Hulstrom RL, Lewis LJ (1983) Sol Energy 30:563. doi:10.1016/0038-092X(83)90068-3

11. Fujishima A, Honda K (1972) Nature 238:37. doi:10.1038/238037a0
12. Aroutiounian VM, Arakelyan VM, Shahnazaryan GE (2005) Sol Energy 78:581. doi:10.1016/j.solener.2004.02.002
13. Kudo A (2007) Int J Hydrogen Energy 32:2673. doi:10.1016/j.ijhydene.2006.09.010
14. Shangguan W (2007) Sci Technol Adv Mater 8:76. doi:10.1016/j.stam.2006.09.007
15. Ni M, Leung MKH, Leung DYC, Sumathy K (2007) Renew Sustain Energy Rev 11:401. doi:10.1016/j.rser.2005.01.009
16. Park JH, Kim SW, Bard AJ (2006) Nano Lett 6:24. doi:10.1021/nl051807y
17. Qian X, Qin D, Song Q, Bai Y, Li T, Tang X et al (2001) Thin Solid Films 385:152. doi:10.1016/S0040-6090(01)00771-4
18. Khan SUM, Sultana T (2003) Sol Energy Mater Sol Cells 76:211. doi:10.1016/S0927-0248(02)00394-X
19. Park JH, Park OOK, Kim SW (2006) Appl Phys Lett 89:163106. doi:10.1063/1.2357878
20. Xu C, Shaban YA, Ingler WB Jr, Khan SUM (2007) Sol Energy Mater Sol Cells 91:938. doi:10.1016/j.solmat.2007.02.010
21. Xie Y (2006) Electrochim Acta 51:3399. doi:10.1016/j.electacta.2005.10.003
22. Misra M, Raja KS, Mahajan VK, Mohapatra SK (2006) In: Vayssieres L (ed) Solar hydrogen and nanotechnology: Proc. of SPIE, vol 6340, p 63400I
23. Khan SUM, Al-Shahry M, Ingler WB Jr (2002) Science 27:2243. doi:10.1126/science.1075035
24. Macak JM, Tsuchiya H, Berger S, Bauer S, Fujimoto S, Schmuki P (2006) Chem Phys Lett 428:421. doi:10.1016/j.cplett.2006.07.062
25. Mor GK, Shankar K, Paulose M, Varghese OK, Grimes CA (2005) Nano Lett 5:191. doi:10.1021/nl048301 k
26. Lana-Villarreal T, Gomez R (2005) Electrochem Commun 7:1218. doi:10.1016/j.elecom.2005.08.031
27. Lana-Villarreal T, Gomez R (2005) Chem Phys Lett 414:489. doi:10.1016/j.cplett.2005.08.117
28. Ikuma Y, Bessho H (2007) Int J Hydrogen Energy 32:2689. doi:10.1016/j.ijhydene.2006.09.024
29. Trenczek-Zajac A, Radecka M, Rekas M (2007) Physica B (Amsterdam) 399:55. doi:10.1016/j.physb.2007.05.021
30. Paulose M, Prakasam HE, Varghese OK, Peng L, Popat KC, Mor GK et al (2007) J Phys Chem C 111:14992. doi:10.1021/jp075258r
31. Shankar K, Mor GK, Prakasam HE, Yoriya S, Paulose M, Varghese OK, Grimes CA (2007) Nanotechnology 18:065707
32. Prakasam HE, Shankar K, Paulose M, Varghese OK, Grimes CA (2007) J Phys Chem C 111:7235. doi:10.1021/jp070273 h
33. O'Regan B, Grätzel M (1991) Nature 353:737. doi:10.1038/353737a0
34. Grätzel M (2001) Nature 414:338. doi:10.1038/35104607
35. Nazeeruddin MK, Kay A, Rodicio I, Humphry-Baker R, Muller E, Liska P et al (1993) J Am Chem Soc 115:6382. doi:10.1021/ja00067a063
36. Nazeeruddin MK, Humphry-Baker R, Officer DL, Campbell WM, Burrell AK, Grätzel M (2004) Langmuir 20:6514. doi:10.1021/la0496082
37. Campbell WM, Jolley KW, Wagner P, Wagner K, Walsh PJ, Gordon KC et al (2007) J Phys Chem C 111:11760. doi:10.1021/jp0750598
38. Wang Q, Campbell WM, Bonfantani EE, Jolley KW, Officer DL, Walsh PJ et al (2005) J Phys Chem B 109:15397. doi:10.1021/jp052877w
39. Ishibashi K, Yamaguchi R, Kimura Y, Niwano M (2008) J Electrochem Soc 155:K10. doi:10.1149/1.2801975
40. Peter LM, Ponomarev EA, Franco G, Shaw NJ (1999) Electrochim Acta 45:549. doi:10.1016/S0013-4686(99)00233-9
41. Peter LM, Riley DJ, Tull EJ, Wijayantha KGU (2002) Chem Commun (Camb):1030. doi:10.1039/b201661c
42. Wijayantha KGU, Peter LM, Otley LC (2004) Sol Energy Mater Sol Cells 83:363. doi:10.1016/j.solmat.2003.12.011
43. Riley DJ, Waggett JP, Wijayantha KGU (2004) J Mater Chem 14:704. doi:10.1039/b311517 h
44. Peter LM, Wijayantha KGU, Riley DJ, Waggett JP (2003) J Phys Chem B 107:8378. doi:10.1021/jp030334 1
45. Cameron PJ, Peter LM, Zakeeruddin SM, Grätzel M (2004) Coord Chem Rev 248:1447. doi:10.1016/j.ccr.2004.02.010
46. Cameron PJ, Peter LM (2003) J Phys Chem B 107:14394. doi:10.1021/jp030790±
47. Doherty RP, Hickey SG, Riley DJ, Tull EJ (2004) J Electroanal Chem 569:271. doi:10.1016/j.jelechem.2004.03.009
48. Li Q, Chen L, Lu G (2007) J Phys Chem C 111:11494. doi:10.1021/jp072520n
49. Ou Y, Lin J, Fang S, Liao D (2006) Chem Phys Lett 429:199. doi:10.1016/j.cplett.2006.08.024
50. Lindgren T, Wang H, Beermann N, Vayssieres L, Hagfeldt A, Lindquist S (2002) Sol Energy Mater Sol Cells 71:231. doi:10.1016/S0927-0248(01)00062-9
51. Glasscock JA, Barnes PRF, Plumb IC, Bendavid A, Martin PJ (2006) In: Vayssieres L (ed) Solar Hydrogen and Nanotechnology: Proc. of SPIE, vol 6340, p 63400N
52. Barnes PRF, Blake D, Glasscock JA, Plumb IC, Vohralik PF, Bendavid A et al (2006) In: Vayssieres L (ed) Solar Hydrogen and Nanotechnology: Proc. of SPIE, vol 6340, p 63400P
53. Kennedy JH, Anderman M (1983) J Electrochem Soc 130(4):848. doi:10.1149/1.2119833
54. Augustynski J, Solarska R, Hagemann H, Santato C (2006) In: Vayssieres L (ed) Solar Hydrogen and Nanotechnology: Proc. of SPIE, vol 6340, p 63400J
55. Nakato Y, Kato N, Imanishi A, Sugiura T, Ogawa S, Yoshida N, et al (2006) In: Vayssieres L (ed) Solar Hydrogen and Nanotechnology: Proc. of SPIE, vol 6340, p 63400U
56. Maeda K, Teramura K, Lu D, Takata T, Saito N, Inoue Y et al (2006) Nature 440:295. doi:10.1038/440295a
57. Maeda K, Teramura K, Takata T, Hara M, Saito N, Toda K et al (2005) J Phys Chem B 109:20504. doi:10.1021/jp053499y
58. Ritterskamp P, Kuklya A, Wustkamp M, Kerpen K, Weidenthaler C, Demuth M (2007) Angew Chem Int Ed 46:7770. doi:10.1002/anie.200701626
59. Yamada S, Nosaka AY, Nosaka Y (2005) J Electroanal Chem 585:105. doi:10.1016/j.jelechem.2005.07.025
60. Sasaki T, Ebina Y, Fukuda K, Tanaka T, Harada M, Watanabe M (2002) Chem Mater 14:3524. doi:10.1021/cm0202456
61. Shangguan W, Yoshida A (2001) Sol Energy Mater Sol Cells 69:189. doi:10.1016/S0927-0248(01)00020-4
62. Tian M, Shangguan W, Yuan J, Jiang L, Chen M, Shi J et al (2006) Appl Catal Gen 309:76. doi:10.1016/j.apcata.2006.04.035
63. Kruger P (2006) Alternative energy resources—a quest for sustainable energy. Wiley, New Jersey
64. Ross DK (2006) Vacuum 80:1084. doi:10.1016/j.vacuum.2006.03.030
65. Sakintuna B, Lamari-Darkrim F, Hirscher M (2007) Int J Hydrogen Energy 32:1121. doi:10.1016/j.ijhydene.2006.11.022
66. Dornheim M, Eigen N, Barkhordarian G, Klassen T, Bormann R (2006) Adv Eng Mater 8:377. doi:10.1002/adem.200600018
67. Liang G, Huot J, Boily S, Van Neste A, Schulz R (1999) J Alloy Compd 292:247. doi:10.1016/S0925-8388(99)00442-9
68. Hanada N, Ichikawa T, Fujii H (2005) J Phys Chem B 109:7188. doi:10.1021/jp044576c
69. Huot J, Liang G, Schulz R (2001) Appl Phys A 72:187
70. Zaluska A, Zaluski L, Ström-Olsen JO (2001) Appl Phys A 72:157

71. Varin RA, Czujko T, Wronski Z (2006) Nanotechnology 17: 3856. doi:10.1088/0957-4484/17/15/041
72. Varin RA, Czujko T, Chiu C, Wronski Z (2006) J Alloy Compd 424:356. doi:10.1016/j.jallcom.2005.12.087
73. Zaluska A, Zaluski L, Strom–Olsen JO (1999) J Alloy Compd 288:217. doi:10.1016/S0925-8388(99)00073-0
74. Zaluska A, Zaluski L, Strom-Olsen JO (1999) J Alloy Compd 289:197. doi:10.1016/S0166-0462(99)00013-7
75. Huot J, Liang G, Boily S, Van Neste A, Schulz R (1999) J Alloy Compd 293–295:495. doi:10.1016/S0925-8388(99)00474-0
76. Kwon IH, Bobet JL, Bae JS, Song MY (2005) J Alloy Compd 396:264. doi:10.1016/j.jallcom.2004.12.036
77. Huot J (2003) In: Nalwa HS (ed) Nanoclusters and nanocrystals. American Scientific Publishers, CA
78. Huot J, Akiba E, Takada T (1995) J Alloy Compd 231:815. doi: 10.1016/0925-8388(95)01764-X
79. Zeng K, Klassen T, Oelerich W, Bormann R (1999) J Alloy Compd 283:213. doi:10.1016/S0925-8388(98)00902-5
80. Tessier P, Akiba E (2000) J Alloy Compd 302:215. doi: 10.1016/S0925-8388(99)00684-2
81. Hanada N, Ichikawa T, Fujii H (2005) J Alloy Compd 404–406:716. doi:10.1016/j.jallcom.2004.12.166
82. Bobet J-L, Chevalier B, Darriet B (2002) J Alloy Compd 330–332:738. doi:10.1016/S0925-8388(01)01580-8
83. Liang G, Huot J, Boily S, Van Neste A, Schulz R (1999) J Alloy Compd 291:295. doi:10.1016/S0925-8388(99)00268-6
84. Liang G, Huot J, Boily S, Schulz R (2000) J Alloy Compd 305:239. doi:10.1016/S0925-8388(00)00708-8
85. Reule H, Hirscher M, Weißhardt A, Kronmuller H (2000) J Alloy Compd 305:246. doi:10.1016/S0925-8388(00)00710-6
86. Wang P, Zhang HF, Ding BZ, Hu ZQ (2000) J Alloy Compd 313:209. doi:10.1016/S0925-8388(00)01186-5
87. Wang P, Wang AM, Wang YL, Zhang HF, Hu ZQ (2000) Scr Mater 43:83. doi:10.1016/S1359-6462(00)00370-5
88. Gennari FC, Castro FJ, Urretavizcaya G (2001) J Alloy Compd 321:46. doi:10.1016/S0925-8388(00)01460-2
89. Au M (2005) Mater Sci Eng B 117:37. doi:10.1016/j.mseb.2004.10.017
90. Tsuda M, Dino WA, Kasai H, Nakanishi H, Aikawa H (2006) Thin Solid Films 509:157. doi:10.1016/j.tsf.2005.09.139
91. Liu FJ, Suda S (1996) J Alloy Compd 232:212. doi:10.1016/0925-8388(95)01931-6
92. Xie L, Liu Y, Wang YT, Zheng J, Li XG (2007) Acta Math 55:4585. doi:10.1016/j.actamat.2007.04.020
93. Vegge T (2004) Phys Rev 70:035412
94. Du AJ, Smith SC, Yao XD, Lu GQ (2005) J Phys Chem B 109:18037. doi:10.1021/jp052804c
95. Jin SA, Shim JH, Ahn JP, Cho YW, Yi KW (2007) Acta Math 55:5073. doi:10.1016/j.actamat.2007.05.029
96. Wu CZ, Wang P, Yao X, Liu C, Chen DM, Lu GQ et al (2006) J Alloy Compd 420:278. doi:10.1016/j.jallcom.2005.10.028
97. Wu CZ, Wang P, Yao XD, Liu C, Chen DM, Lu GQ et al (2006) J Alloy Compd 414:259. doi:10.1016/j.jallcom.2005.07.021
98. Yao XD, Wu CZ, Du A, Lu GQ, Cheng HM, Smith SC et al (2006) J Phys Chem B 110:11697. doi:10.1021/jp057526w
99. Du AJ, Smith SC, Yao XD, He Y, Lu GQ (2006) J Phys Conf Ser 29:167. doi:10.1088/1742-6596/29/1/032
100. Luo Y, Wang P, Ma LP, Cheng HM (2007) Scr Mater 56:765. doi:10.1016/j.scriptamat.2007.01.016
101. Imamura H, Sakasai N, Fujinaga T (1997) J Alloy Compd 253–254:34. doi:10.1016/S0925-8388(96)03074-5
102. Imamura H, Sakasai N, Kajii Y (1996) J Alloy Compd 232:218. doi:10.1016/0925-8388(95)01882-4
103. Imamura H, Sakasai N (1995) J Alloy Compd 231:810. doi: 10.1016/0925-8388(95)01722-4
104. Imamura H, Kitazawa I, Tanabe Y, Sakata Y (2007) Int J Hydrogen Energy 32:2408. doi:10.1016/j.ijhydene.2006.10.058
105. Huang ZG, Guo ZP, Calka A, Wexler D, Liu HK (2007) Mater Lett 61:3163. doi:10.1016/j.matlet.2006.11.017
106. Huot J, Pelletier JF, Liang G, Sutton M, Schulz R (2002) J Alloy Compd 330–332:727. doi:10.1016/S0925-8388(01)01662-0
107. Pelletier JF, Huot J, Sutton M, Schulz R, Sandy AR, Lurio LB, Mochrie GJ (2001) Phys Rev B 63:052103
108. Oelerich W, Klassen T, Bormann R (2001) J Alloy Compd 315:237. doi:10.1016/S0925-8388(00)01284-6
109. Oelerich W, Klassen T, Bormann R (2001) J Alloy Compd 322:L5. doi:10.1016/S0925-8388(01)01173-2
110. Barkhordarian G, Klassen T, Bormann R (2004) J Alloy Compd 364:242. doi:10.1016/S0925-8388(03)00530-9
111. Barkhordarian G, Klassen T, Bormann R (2006) J Alloy Compd 407:249. doi:10.1016/j.jallcom.2005.05.037
112. Aguey-Zinsou KF, Fernandez JRA, Klassen T, Bormann R (2007) Int J Hydrogen Energy 32:2400. doi:10.1016/j.ijhydene.2006.10.068
113. Li Q, Xu KD, Chou KC, Lin Q, Zhang JY, Lu XG (2005) Intermetallics 13:1190. doi:10.1016/j.intermet.2005.03.006
114. Liu Z, Lei ZL (2007) J Alloy Compd 443:121. doi:10.1016/j.jallcom.2006.09.130
115. Gutfleisch O, Schlorke-de Boer N, Ismail N, Herrich M, Walton A, Speight J et al (2003) J Alloy Compd 356–357:598. doi: 10.1016/S0925-8388(02)01283-5
116. Singh S, Eijt SWH, Zandbergen MW, Legerstee WJ, Svetchnikov VL (2007) J Alloy Compd 441:344. doi:10.1016/j.jallcom.2006.09.108
117. Pranevicius L, Milcius D, Pranevicius LL, Templier C, Bobrovaite B, Barnackas I (2006) Appl Surf Sci 252:4202. doi: 10.1016/j.apsusc.2005.06.034
118. Bérubé V, Radtke G, Dresselhaus M, Chen G (2007) Int J Energy Res 31:637. doi:10.1002/er.1284
119. Yao X, Zhu ZH, Cheng HM, Lu GQ (2008) J Mater Res 23:336. doi:10.1557/jmr.2008.0063
120. Holtz RL, Imam MA (1997) J Mater Sci 32:2267. doi:10.1023/A:1018572116447
121. Wronski Z, Varin RA, Chiu C, Czujko T, Calka A (2007) J Alloy Compd 434–435:743. doi:10.1016/j.jallcom.2006.08.301
122. Bobet JL, Even C, Nakamura Y, Akiba E, Darriet B (2000) J Alloy Compd 298:279. doi:10.1016/S0925-8388(99)00628-3
123. Bobet JL, Akiba E, Nakamura Y, Darriet B (2000) Int J Hydrogen Energy 25:987. doi:10.1016/S0360-3199(00)00002-1
124. Bobet JL, Akiba E, Darriet B (2001) Int J Hydrogen Energy 26:493. doi:10.1016/S0360-3199(00)00082-3
125. Huot J, Tremblay ML, Schulz R (2003) J Alloy Compd 356–357:603. doi:10.1016/S0925-8388(03)00120-8
126. Liu D, Zhu Y, Li L (2007) Int J Hydrogen Energy 32:2455. doi: 10.1016/j.ijhydene.2006.09.037
127. Saita I, Li L, Saito K, Akiyama T (2003) J Alloy Compd 356–357:490. doi:10.1016/S0925-8388(03)00230-5
128. Eigen N, Keller C, Dornheim M, Klassen T, Bormann R (2007) Scr Mater 56:847. doi:10.1016/j.scriptamat.2007.01.024
129. Benard P, Chahine R (2007) Scr Mater 56:803. doi:10.1016/j.scriptamat.2007.01.008
130. Hirscher M, Panella B (2007) Scr Mater 56:809. doi:10.1016/j.scriptamat.2007.01.005
131. Saeyed AM, Antonelli DM (2004) Adv Mater 16(9–10):765
132. Thomas KM (2007) Catal Today 120:389. doi:10.1016/j.cattod.2006.09.015
133. Rowsell JLC, Yaghi OM (2004) Microporous Mesoporous Mater 73:3. doi:10.1016/j.micromeso.2004.03.034
134. Collins DJ, Zhou HC (2007) J Mater Chem 17:3154. doi: 10.1039/b702858j

135. Rossi NL, Eckert J, Eddaoudi M, Vodak DT, Kim J, O'Keeffe M, Yaghi OM (2003) Science 300:1127. doi:10.1126/science.1083440
136. Rowsell JLC, Millward AR, Park KY, Yaghi OM (2004) J Am Chem Soc 126:5666. doi:10.1021/ja049408c
137. Hirscher M, Panella B (2005) J Alloy Compd 404–406:399. doi:10.1016/j.jallcom.2004.11.109
138. Panella B, Hirscher M, Pütter H, Müller U (2006) Adv Funct Mater 16:520. doi:10.1002/adfm.200500561
139. Yildirim T, Hartman MR (2005) Phys Rev Lett 95:215504. doi:10.1103/PhysRevLett.95.215504
140. Yang Q, Zhong C (2006) J Phys Chem B-Lett 110:655. doi:10.1021/jp055908w
141. Kim D, Kim J, Jung DH, Lee TB, Choi SB, Yoon JH et al (2007) Catal Today 120:317. doi:10.1016/j.cattod.2006.09.029
142. Li Y, Yang RT (2006) J Am Chem Soc 128:726. doi:10.1021/ja056831s
143. Li Y, Yang RT (2006) J Am Chem Soc 128:8136. doi:10.1021/ja061681m
144. Lin X, Jia J, Zhao X, Thomas KM, Blake AJ, Walker GS et al (2006) Angew Chem Int Ed 45:7358. doi:10.1002/anie.200601991
145. Surble S, Millange F, Serre C, Duren T, Latroche M, Bourrelly S et al (2006) J Am Chem Soc 128:14889. doi:10.1021/ja064343u
146. Liu Y, Eubank JF, Cairns AJ, Eckert J, Kravtsov VC, Luebke R et al (2007) Angew Chem Int Ed 46:3278. doi:10.1002/anie.200604306
147. Krawiec P, Kramer M, Sabo M, Kunschke R, Fröde H, Kaskel S (2006) Adv Eng Mater 8:293. doi:10.1002/adem.200500223
148. Han SS, Deng WQ, Goddard WAIII (2007) Angew Chem Int Ed 46:6289. doi:10.1002/anie.200700303
149. Wong-Foy AG, Matzger AJ, Yaghi OM (2006) J Am Chem Soc 128:3494. doi:10.1021/ja058213 h
150. Furukawa H, Miller MA, Yaghi OM (2007) J Mater Chem 17:3197. doi:10.1039/b703608f
151. Rowsell JLC, Yaghi OM (2005) Angew Chem Int Ed 44:4670. doi:10.1002/anie.200462786
152. Mueller U, Schubert M, Teich F, Puetter H, Schierle-Arndt K, Pastre J (2006) J Mater Chem 16:626. doi:10.1039/b511962f
153. Muller U, Putter H, Heese M, Wessel W 2005 German Patent:10355087
154. Banerjee S, Murad S, Puri IK (2006) Proc IEEE 94:1806. doi:10.1109/JPROC.2006.883703
155. Chambers A, Park C, Baker RTK, Rodriguez NM (1998) J Phys Chem B 102:4253. doi:10.1021/jp9801141
156. Hirscher M, Becher M, Haluska M, Quintel A, Skakalova V, Choi YM et al (2002) J Alloy Compd 330–332:654. doi:10.1016/S0925-8388(01)01643-7
157. Fan YY, Liao B, Liu M, Wei YL, Lu MQ, Cheng HM (1999) Carbon 37:1649. doi:10.1016/S0008-6223(99)00165-7
158. Gupta BK, Awasthi K, Srivastava ON (2000) Proceedings of the 13th world hydrogen energy conferencce. Hydrogen Energy Progress, vol XIII, p 487
159. Zhou L, Zhou Y, Sun Y (2006) Int J Hydrogen Energy 31:259. doi:10.1016/j.ijhydene.2005.04.048
160. Panella B, Hirscher M, Roth S (2005) Carbon 43:2209. doi:10.1016/j.carbon.2005.03.037
161. Ahn CC, Ye Y, Ratnakumar BV, Witham C, Bowman RC Jr, Fultz B (1998) Appl Phys Lett 73:3378. doi:10.1063/1.122755
162. Strobel R, Jorissen L, Schliermann T, Trapp V, Schutz W, Bohmhammel K et al (1999) J Power Sources 84:221. doi:10.1016/S0378-7753(99)00320-1
163. Poirier E, Chahine R, Bose TK (2001) Int J Hydrogen Energy 26:831. doi:10.1016/S0360-3199(01)00014-3
164. Chen P, Wu X, Lin J, Tan KL (1999) Science 285:91. doi:10.1126/science.285.5424.91
165. Yang RT (2000) Carbon 38:623. doi:10.1016/S0008-6223(99)00273-0
166. Lueking AD, Yang RT, Rodriguez NM, Baker RTK (2004) Langmuir 20:714. doi:10.1021/la0349875
167. Lueking AD, Pan L, Narayanan DL, Clifford CEB (2005) J Phys Chem B 109:12710. doi:10.1021/jp0512199
168. Blackman JM, Patrick JW, Arenillas A, Shi W, Snape CE (2006) Carbon 44:1376. doi:10.1016/j.carbon.2005.11.015
169. Marella M, Tomaselli M (2006) Carbon 44:1404. doi:10.1016/j.carbon.2005.11.020
170. Hong SE, Kim DK, Jo SM, Kim DY, Chin BD, Lee DW (2007) Catal Today 120:413. doi:10.1016/j.cattod.2006.09.013
171. Xu WC, Takahashi K, Matsuoa Y, Hattoria Y, Kumagai M, Ishiyama S et al (2007) Int J Hydrogen Energy 32:2504. doi:10.1016/j.ijhydene.2006.11.012
172. Gupta BK, Tiwari RS, Srivastava ON (2004) J Alloy Compd 381:301. doi:10.1016/j.jallcom.2004.03.094
173. Li J, Furuta T, Goto H, Ohashi T, Fujiwara Y, Yip S (2003) J Chem Phys 119:2376. doi:10.1063/1.1582831
174. Dillon AC, Jones KM, Bekkedahl TA, Kiang CH, Bethune DS, Hebben MJ (1997) Nature 386:377. doi:10.1038/386377a0
175. Ye Y, Ahn CC, Witham C, Fultz B, Liu J, Rinzler AG et al (1999) Appl Phys Lett 74:2307. doi:10.1063/1.123833
176. Liu C, Fan YY, Liu M, Cong HT, Cheng HM, Dresselhaus MS (1999) Science 286:1127. doi:10.1126/science.286.5442.1127
177. Zuttel A, Sudan P, Mauron P, Wenger P (2004) Appl Phys A 78:941. doi:10.1007/s00339-003-2412-1
178. Zacharia R, Kim KY, Hwang SW, Nahm KS (2007) Catal Today 120:426. doi:10.1016/j.cattod.2006.09.026
179. Jorda-Beneyto M, Suarez-Garcia F, Lozano-Castello D, Cazorla-Amoros D, Linares-Solano A (2007) Carbon 45:293. doi:10.1016/j.carbon.2006.09.022
180. Chen CH, Huang CC (2007) Int J Hydrogen Energy 32:237. doi:10.1016/j.ijhydene.2006.03.010
181. Wu XB, Chen P, Lin J, Tan KL (2000) Int J Hydrogen Energy 25:261. doi:10.1016/S0360-3199(99)00037-3
182. Costa PMFJ, Coleman KS, Green MLH (2005) Nanotechnology 16:512. doi:10.1088/0957-4484/16/4/030
183. Shiraishi M, Takenobu T, Yamada A, Ata M, Kataura H (2002) Chem Phys Lett 358:213. doi:10.1016/S0009-2614(02)00525-0
184. Johansson E, Hjorvarsson B, Ekstrom T, Jacob M (2002) J Alloy Compd 330–332:670. doi:10.1016/S0925-8388(01)01641-3
185. Zuttel A, Nutzenadel C, Sudan P, Mauron P, Emmenegger C, Rentsch S et al (2002) J Alloy Compd 330–332:676. doi:10.1016/S0925-8388(01)01659-0
186. Zhou L, Zhou Y, Sun Y (2004) Int J Hydrogen Energy 29:475. doi:10.1016/S0360-3199(03)00092-2
187. Pinkerton FE, Wicke BG, Olk CH, Tibbetts GG, Meisner GP, Meyer MS et al (2000) J Phys Chem B 104:9460. doi:10.1021/jp000957o
188. Yang FH, Lachawiec AJ Jr, Yang RT (2006) J Phys Chem B 110:6236. doi:10.1021/jp056461u
189. Lueking AD, Yang RT (2004) Appl Catal A 265:259. doi:10.1016/j.apcata.2004.01.019
190. Zacharia R, Kim KY, Fazle Kibria AKM, Nahm KS (2005) Chem Phys Lett 412:369. doi:10.1016/j.cplett.2005.07.020
191. Rather S, Zacharia R, Hwang SW, Naik M, Nahm KS (2007) Chem Phys Lett 441:261. doi:10.1016/j.cplett.2007.05.006
192. Anson A, Lafuente E, Urriolabeitia E, Navarro R, Benito AM, Maser WK et al (2007) J Alloy Compd 436:294. doi:10.1016/j.jallcom.2006.07.026
193. Kowalczyk P, Brualla L, Żywociński A, Bhatia SK (2007) J Phys Chem C 111:5250. doi:10.1021/jp068484u
194. Cao D, Wang WC (2007) Int J Hydrogen Energy 32:1939. doi:10.1016/j.ijhydene.2006.08.028

195. Ye X, Gu X, Gong XG, Shing TKM, Liu ZF (2007) Carbon 45:315. doi:10.1016/j.carbon.2006.09.026
196. Zhang C, Lu XS, Gu AZ (2004) Int J Hydrogen Energy 29:1271. doi:10.1016/j.ijhydene.2003.12.001
197. Lamari Darkrim F, Malbrunota P, Tartaglia GP (2002) Int J Hydrogen Energy 27:193. doi:10.1016/S0360-3199(01)00103-3
198. Kiyobayashi T, Takeshita HT, Tanaka H, Takeichi N, Zuttel A, Schlapbach L et al (2002) J Alloy Compd 330–332:666. doi:10.1016/S0925-8388(01)01436-0
199. Viculis LM, Mack JJ, Kaner RB (2003) Science 299:1361. doi:10.1126/science.1078842
200. Braga SF, Coluci VR, Baughman RH, Galvao DS (2007) Chem Phys Lett 441:78. doi:10.1016/j.cplett.2007.04.060
201. Braga SF, Coluci VR, Legoas SB, Giro R, Galvao DS, Baughman RH (2004) Nano Lett 4:881. doi:10.1021/nl0497272
202. Mpourmpakis G, Tylianakis E, Froudakis GE (2007) Nano Lett 7:1893. doi:10.1021/nl070530u
203. Iijima S (1991) Nature 354:56. doi:10.1038/354056a0
204. Guo T, Nikolaev P, Rinzler AG, Tománek D, Colbert DT, Smalley RE (1995) J Phys Chem 99:10694. doi:10.1021/j100027a002
205. Guo T, Nikolaev P, Thess A, Colbert DT, Smalley RE (1995) Chem Phys Lett 243:49. doi:10.1016/0009-2614(95)00825-O
206. José-Yacamán M, Miki-Yoshida M, Rendón L, Santiesteban JG (1993) Appl Phys Lett 62:657. doi:10.1063/1.108857
207. Jhi SH, Kwon YK, Bradley K, Gabriel JCP (2004) Solid State Commun 129:769. doi:10.1016/j.ssc.2003.12.032
208. Guo ZP, Yuan L, Konstantinov K, Huang ZG, Liu HK (2006) Mater Lett 60:3891. doi:10.1016/j.matlet.2006.03.135
209. Wang J, Nelson JA, White WB, Eklund PC, Adair JH (2006) Mater Lett 60:3573. doi:10.1016/j.matlet.2006.03.062
210. Jhi SH, Kwon YK (2004) Phys Rev B 69:245407. doi:10.1103/PhysRevB.69.245407
211. Jhi SH, Kwon YK (2005) Phys Rev B 71:035408. doi:10.1103/PhysRevB.71.035408
212. Wang L, Major D, Paga P, Zhang D, Norton MG, McIlroy DN (2006) Nanotechnology 17:S298. doi:10.1088/0957-4484/17/11/S12
213. Chen M, Xing YC (2005) Langmuir 21:9334. doi:10.1021/la051892p
214. Fagley J, Conley J, Masten D (2005) Proceedings of FUELCELL—third international conference on fuel cell science, engineering and technology, p 613
215. Stevens DA, Dahn JR (2003) J Electrochem Soc 150:A770. doi:10.1149/1.1573195
216. Alvisi M, Galtieri G, Giorgi L, Giorgi R, Serra E, Signore MA (2005) Surf Coat Tech 200:1325. doi:10.1016/j.surfcoat.2005.07.093
217. Radev I, Slavcheva E, Budevski E (2007) Int J Hydrogen Energy 32:872. doi:10.1016/j.ijhydene.2007.01.015
218. Zeis R, Mathur A, Fritz G, Lee J, Erlebacher J (2007) J Power Sources 165:65. doi:10.1016/j.jpowsour.2006.12.007
219. Bron M, Radnik J, Fieber-Erdmann M, Bogdanoff P, Fiechter S (2002) J Electroanal Chem 535:113. doi:10.1016/S0022-0728(02)01189-0
220. Bron M, Fiechter S, Bogdanoff P, Tributsch H (2002) Fuel Cells Fundam Syst 2:137. doi:10.1002/fuce.200290012
221. Matter PH, Ozkan US (2006) Catal Lett 109:115. doi:10.1007/s10562-006-0067-1
222. Matter PH, Zhang L, Ozkan US (2006) J Catal 239:83. doi:10.1016/j.jcat.2006.01.022
223. Matter PH, Wang E, Arias M, Biddinger EJ, Ozkan US (2007) J Mol Catal Chem 264:73. doi:10.1016/j.molcata.2006.09.008
224. Liu Z, Gan LM, Hong L, Chen W, Lee JY (2005) J Power Sources 139:73. doi:10.1016/j.jpowsour.2004.07.012
225. Girishkumar G, Rettker M, Underhile R, Binz D, Vinodgopal K, McGinn P et al (2005) Langmuir 21:8487. doi:10.1021/la051499j
226. Glora M, Wiener M, Petričević R, Pröbstle H, Fricke J (2001) J Non-Cryst Solids 285:283. doi:10.1016/S0022-3093(01)00468-9
227. Caillard A, Charles C, Boswell R, Brault P (2007) Nanotechnology 18:305603. doi:10.1088/0957-4484/18/30/305603
228. Yuan F, Ryu H (2004) Nanotechnology 15:S596. doi:10.1088/0957-4484/15/10/017
229. Mukerjee S, Lee SJ, Ticianelli EA, McBreen J, Grgur BN, Markovic NM et al (1999) Electrochem Solid-State Lett 2:12. doi:10.1149/1.1390718
230. Smitha B, Sridhar S, Khan AA (2005) J Membr Sci 259:10. doi:10.1016/j.memsci.2005.01.035
231. Watanabe M, Uchida H, Emori M (1998) J Phys Chem B 102:3129. doi:10.1021/jp973477e
232. Uchida H, Ueno Y, Hagihara H, Watanabe M (2003) J Electrochem Soc 150:A57. doi:10.1149/1.1523412
233. Chen SY, Han CC, Tsai CH, Huang J, Chen-Yang YW (2007) J Power Sources 171:363. doi:10.1016/j.jpowsour.2007.06.047
234. Ekstrom H, Wickman B, Gustavsson M, Hanarp P, Eurenius L, Olsson E et al (2007) Electrochim Acta 52:4239. doi:10.1016/j.electacta.2006.12.002
235. Jalani NH, Datta R (2005) J Membr Sci 264:167. doi:10.1016/j.memsci.2005.04.047
236. Jalani NH, Dunn K, Datta R (2005) Electrochim Acta 51:553. doi:10.1016/j.electacta.2005.05.016
237. Choi P, Jalani NH, Thampan TM, Datta R (2006) J Polymer Sci. Part B Polym Phys 44:2183. doi:10.1002/polb.20858